SOLIDS BY DESIGN: EXPLORING VARIATIONS IN SURFACE CHEMISTRY AND NANOSTRUCTURE ORIENTATION IN THE DESIGN OF FUNCTIONAL NANOCRYSTAL SOLIDS

A Thesis

Presented to the Faculty of the Graduate School

of Cornell University

In Partial Fulfillment of the Requirements for the Degree of

Master of Science

by

Christian Hwang Ocier

May 2014

ABSTRACT

Engineering functional solids from nanocrystalline building blocks presents a novel approach to design new, solution processed functional materials and devices. When NCs organize into an assembly, the interactions between these materials can be modified depending on their surface chemistry and nanostructure orientation, two parameters that are explored in this dissertation.

The overarching goal in studies that explore alternative surface chemistries for colloidal nanocrystals is to replace the long, insulating organic ligands that cover the particle surface during synthesis with short, preferably inorganic molecules that facilitate more efficient dot-to-dot interactions. The ligand chemistry I studied for the surface chemistry project uses chalcogenidometallate clusters (ChaMs), inorganic metal chalcogenide ions that can collapse to form a mesoporous semiconductor film around a nanocrystal array. Previous reports indicate that this material can coordinate with the surface of NCs like CdSe to form all-inorganic nanocomposites for electronic devices. Due to the labile surface chemistry of PbSe, this approach is unfeasible, requiring instead a solid exchange that allows the ChaMs to infiltrate and replace the organic ligands in deposited films of PbSe NCs. The success of our ligand exchange approach is attributed to the processing conditions that allow PbSe NCs to retain their nanocrystalline character even when exposed to the caustic ChaMs. After surface treatment and annealing, the inorganic nanocomposites exhibit function as electronic materials for NC-based transistor devices.

Another consideration in the design of NC solids is the structural orientation

that each building blocks assume within a film. The effects of structural orientation are especially evident in anisotropic materials like nanorods, where the geometry of the building block defines the direction in which optical and electronic properties are more pronounced. I monitored the self-assembly of CdSe/CdS NRs in a solvent vapor cell using GISAXS and GIWAXS to probe film structure and optical transmission to correlate material orientation with absorption. Ex-situ photoluminescence measurements were collected to support our in-situ measurements. We determined that absorption is most pronounced when the nanostructure long axis is perpendicular to the direction of light, a result which can be explained by ex-situ measurements and simulations.

BIOGRAPHICAL SKETCH

Christian Ocier obtained a B.S. in chemical engineering and an additional major in chemistry in 2009. After completing his undergraduate studies, he moved to Beijing, China to undertake a research position with the Tsinghua University materials science department as a visiting researcher. While there, he explored synthetic methods to prepare colloidal nanocrystals of magnetic oxides, metals, and hybrid structures that can be incorporated into exploratory magnetic devices. In the fall of 2011, Christian moved to Cornell University to pursue an M.S. in materials science with the Robinson and Hanrath groups, focusing on exploring different methods for functionalizing nanocrystal solids for novel optoelectronic devices. The research he performed during his master's degree is presented in this dissertation. After finishing his M.S. degree, Christian moved to Urbana, Illinois, where he is currently a research scientist with the Braun group, this time investigating questions of self-assembly and nanostructure modification for the preparation of three dimensional optical materials.

To my grandparents Robert and Lily, who granted me this tremendous opportunity to reboot my career as a materials scientist. Thank you for your unwavering support, your love, and your encouragement.

ACKNOWLEDGMENTS

My gratitude and appreciation must first go to my advisers Richard Robinson and Tobias Hanrath. Professor Robinson's training and methodology stands as a paragon of how the pursuit of scientific ideas from inception to publication ought to be approached. Professor Hanrath is an example of an adviser whose infectious passion for the rapidly evolving nature of nanoscience and whose unflagging energy can drive agendas and collaborations forward. Thank you Professors Robinson and Hanrath for the help, the advice, the guidance, and all the resources you provided during my master's degree.

The inspiration for this project, some samples and materials, and the many stimulating discussions came from members of the Robinson and Hanrath groups: Liane Moreau, Haitao Zhang, Donhyung Ha, Obafemi Otelaja, Maria Ibanez, Kevin Whitham, and Benjamin Richards. Thank you for the time and the work you invested towards assisting my projects toward completion.

To the CCMR staff, thank you for deepening my understanding of the complex systems I had to examine under your instruments: John Grazul, Don Werder, Mick Thomas, Maura Weathers, Jon Xu, and Steve Kriske, your training and your guidance have provided me a solid foundation for carrying out my experimental work.

To my collaborators at CHESS, Drs. Detlef Smilgies, Matthew Ward, Maggie Koker, and Ernest Fontes, thank you so much for your generosity with your knowledge, your time, and your expertise with my synchrotron experiments. My second project benefited greatly from your help, and my experiences at Cornell have become much richer through working with you.

TABLE OF CONTENTS

LIST OF ABBREVIATIONS

ACN	Acetonitrile
CdS	Cadmium Sulfide
CdSe	Cadmium Selenide
ChaM	Chalcogenidometallate Cluster
CHESS	Cornell High Energy Synchrotron Source
DMSO	Dimethyl Sulfoxide
FET	Field Effect Transistor
FTIR	Fourier Transform Infrared Spectroscopy
GISAXS	Grazing Incidence Small Angle X-ray Scattering
GIWAXS	Grazing Incidence Wide Angle X-ray Scattering
In_2Se_3	Indium Selenide
MCC	Metal Chalcogenide Complex
MPTMS	3-Mercaptopropyltrimethoxysilane
NC	Nanocrystal
NR	Nanorod
PbSe	Lead Selenide
S	Sulfure
SAM	Self-Assembled Monolayer
Se	Selenium
SEM	Scanning Electron Microscope
$SnSe_2$	Tin Selenide
TEM	Transmission Electron Microscope
TOP	Tri-n-octylphosphine
XRD	x-ray diffraction

LIST OF FIGURES

PREFACE

One of the greatest privileges of my graduate school career at Cornell University was working with scientists who were striving to understand questions regarding the fundamental properties and the application of colloidal nanomaterials. Prior to arriving at Cornell, I spent the better part of a year and a half at Beijing's Tsinghua University teaching myself methods to prepare nanocrystals of magnetic oxides. The colloidal nanoscience community has for years recognized the value of constraining the dimensions of conventional materials down to nanoscale sizes to obtain properties unavailable in the bulk. By applying the intuition and the skill of a modern day alchemist, one can combine a variety of metal precursors and solvents to create well dispersed solutions of materials with unusual physical properties and phases. During my first attempt at creating these materials (an iron oxide called maghemite), I drew from the knowledge I obtained as an undergraduate inorganic chemist to prepare an iron-oleate precursor—a dirty and messy endeavor that required hours of applying heat and distillation to a large pot of viscous ingredients. When a scant gram of this maroon mixture was collected, I added sufficient amounts of solvent and heated this mixture to what I then regarded as impossibly high temperatures to nucleate our maghemite nanocrystals. In the absence of any proper air-free paraphernalia, those first attempts at this chemistry resulted in eruptions that coated my workspace in a thin film of tiny little magnets. These inconveniences prompted me to construct a bona fide Schlenk line with parts and scaffolding collected from a variety of interesting little shops in Beijing, and upon its completion, my formal instruction in the art of true colloidal chemistry began.

At Cornell, I became a student of Professors Richard Robinson and Tobias Hanrath, two scientists who had received their training from some of the most prestigious groups in the United States. My first project at Cornell was a synthesis effort that examined how a reactive sulfur precursor can be used to systematically prepare a wide variety of metal chalcogenides. A year later, I contacted Professor Hanrath to embark on a collaboration between both advisers to determine how we can modify the surfaces of lead salt nanocrystals with new surface ligands to improve their performance in optoelectronic devices. I walked into that project little knowing how difficult it was to work with lead salt nanocrystals, or the challenges of fabricating these chemically processed devices. Many of those experiments involved long hours hovering over films that were submerged in highly toxic solutions with anhydrous hydrazine. Many of those experiments also involved devices with gate oxides that leaked, resulting in a space in our glovebox that served as a mass graveyard for defective wafers. After struggling with countless devices that behaved like resistors, we were able to create a number of functional films of these nanocomposites. One couldn't even imagine the relief I experienced knowing that these efforts yielded something of value to the community, and that I would never need to touch rocket fuel ever again.

During the time that I was completing my first project, Professor Hanrath enlisted me to perform some scattering experiments on CdSe/CdS dot-in-rod nanorod films using GISAXS and GIWAXS. This project, which started out as a collaboration between Liberato Manna's group in Italy and ours, aimed to understand the superlattice structure in self-assembled films of colloidal nanorods and to correlate

these structural characteristics with the assembly's optical absorption. Preliminary scattering experiments had been conducted on the rods a year before I joined the Hanrath group, but the patterns we obtained did not resemble closely the orientation dependence of a nanorod assembly. It turned out that we had received unusually shaped crystals that resembled arrows more than rods. Given the Robinson group's expertise and facilities, I synthesized the rods in our own labs and brought them to CHESS during our group's Spring 2013 run. The scattering results that resulted from these rod samples exhibited the characteristic structural properties of nanorod assemblies. The dot-in-rod structure, apart from featuring the striking photoluminescence inherent in core-shell materials, also yielded optical absorption curves that shifted based on the relative orientation of the NRs in an assembly. These effects ultimately describe the structure-property relationship in assemblies of anisotropic nanomaterials.

Having worked with these remarkable nanocrystalline materials has been an incredibly gratifying experience. To have studied the correlations between a material's surface chemistry and its electronic structure, in addition to the superlattice order present in a thin film, has provided me with such a rich breadth of experimental expertise.

CHAPTER ONE

THESIS OVERVIEW

1.1 Surface ligand functionalization of PbSe Nanocomposites

Current solution processed device technologies can be fabricated with chemically synthesized electronic materials like conductive polymers, electronically active small molecules, and more recently, colloidal nanocrystals. Colloidal nanocrystals of semiconductor materials, also known as quantum dots, are inherently electronic materials whose energy levels can be tuned by varying their size and structure during synthesis. Due to their quantum confined optical and electronic properties, quantum dots have become the focus of several groups attempting to integrate them into novel devices. As we push towards increasing the performance of nanocrystal-based optoelectronic device, two important questions arise: how do we select the appropriate ligand chemistry that can improve electronic transport within an NC thin film, and what processing methods can be best employed to incorporate NCs into device architectures? Replacing the native ligands on nanocrystals removes an insulating barrier that will otherwise render a nanocrystal film inert. By using short inorganic molecules to occupy the interfaces within these nanocrystals, conductive films can be fabricated and integrated into optoelectronic devices like field-effect transistors and solar cells.

Surface ligand exchange is conventionally achieved by placing a solution of nanocrystals dispersed in an organic solvent above a polar solvent containing the short ligand molecules. The nanocrystals that straddle the liquid-liquid interface will

migrate across this barrier, and the short molecules will then stabilize the nanocrystals in the polar solvent. Coupling quantum dots using this method offers multiple advantages, such as the direct deposition of close-packed quantum dot films from solution onto substrates, the lack of volume shrinkage, and the ability to directly define the ligand to particle concentration in solution.

Solution exchange, however, cannot be universally applied to all nanocrystal species. The lead chalcogenides, for instance, are susceptible to agglomeration when their native ligands are removed in solution, thereby decreasing the diversity of nanocrystal ligands that can be applied to couple and functionalize lead salt-based NC devices. Since many of the ligand chemistries that have yielded performance devices have been largely applied to CdSe nanocrystals, determining a processing method that will exhibit compatibility with the lead salts will represent a significant improvement for these materials. Lead salts are normally chemically functionalized into close-packed arrays after they are deposited onto substrates. Depending on the chemical environment that these salts are exposed to during ligand replacement, the electronic structure of the material can also be modified. Hence, developing new ligand chemistries for lead salts, despite the several advantages that have been proposed for using the material, remains a challenge from both a chemical and device engineering standpoint.

In Chapter 2, we introduce a study that investigates how PbSe NC films can be chemically functionalized with inorganic molecules called chalcogenidometallate clusters (ChaMs). Although the clusters were previously used to couple CdSe quantum dots for field-effect transistors, the chemical environment of the ChaMs and the

challenges of processing lead salt materials with this chemistry prevented them from being incorporated into function al optoelectronic device. Our study was patterned after a publication from the Milliron group at the Lawrence Berkeley National Labs, which proposed a solid exchange method to replace the oleates with the ChaMs. Chapter 2 introduces a method that replaces these ChaMs without producing too many surface states at the nanocrystal interfaces, rendering these devices as functional field effect transistors. This chapter will deal with the methodology we employ, in addition to the processing steps we systematically studied to ensure that the devices we fabricated yielded consistent electrical behavior.

1.2 Correlating Structure in Nanorod Superlattices with Optical Anisotropy

When highly monodisperse solutions of colloidal nanocrystals could finally be prepared during the early stages of this research field, the crystals could under controlled conditions self-assemble into a superlattice. Among other parameters, size distribution, solvent evaporation, and particle-ligand interactions were critical towards inducing the controlled nucleation of ordered structures. In the recent decade, complex superlattices containing two or three species of nanocrystals were also found to combine and assemble into structures that resemble the atomic lattices of inorganic salts. Depending on the constituent nanocrystal's properties, the nanocrystal superstructure can exhibit varying physical properties that depend on the assembly's order. For instance, when semiconductor nanocrystals like CdSe organize into an array, the photoluminescence of the solid ensemble also shifts depending on the degree of superlattice order assumed by the building blocks. Recently, studies have

suggested that catalytic activity of certain binary nanocrystal mixtures can be enhanced depending on the superlattice order that forms. Given the advantages that arise from these structured materials, determining the mechanisms and the properties that accompany superlattice formation would be advantageous for the rational design of functional nanocrystal solids.

Superlattice structure can also be achieved for anisotropic materials such as nanorods and tetrapods. Due to the challenges in synthesizing highly monodisperse batches of anisotropic colloidal nanomaterials, highly ordered assemblies were only achieved in recent years when the synthetic procedures for these materials were refined. For anisotropic semiconductors like nanorods, the most immediately observable change in superlattice order is related to its optical anisotropy. The photoluminescence of upstanding arrays of cadmium chalcogenide rods, for instance, exhibit polarization dependence about the nanorod axis. Due to the rich optical properties and electron transfer mechanisms that occur in anisotropic materials, determining their mechanisms for self-assembly and finding the optimal conditions for creating functional rod arrays would allow for the consistent fabrication of these solids.

The Hanrath group had previously investigated the structural differences that arise in as-synthesized, treated and air-exposed PbSe colloidal nanocrystal assemblies using grazing incidence diffraction techniques. Our motivation for studying superlattice order CdSe/CdS dot-in-rod structures arises from their optical anisotropy, their ability to nucleate into monodisperse rods when they are synthesized with uniform CdSe seeds, and their visible absorption and emission in the visible spectrum.

In Chapter3, we describe an in-situ study we conducted at CHESS wherein arrays of colloidal CdSe/CdS dot-in-rod structures are assembled into superlattices. We use a technique that is conventionally use d to swell and crystallize polymer films to induce order and disorder within the rod arrays, and prob e the structural properties using grazing incidence diffraction techniques like GISAXS and GIWAXS in concert with in-situ absorption measurements to correlate assembly order with their absorption intensity. These results are then substantiated with ex-situ photoluminescence measurements and theoretical calculations. These experiments directly provide time-resolved evidence that relates the structure-property relationship of anisotropic nanocrystal superlattices, and shows how we can optimally design new solid state nanorod absorbers.

CHAPTER TWO

CHALCOGENIDOMETALLATE CLUSTERS AS SURFACE LIGANDS FOR PbSe FIELD-EFFECT TRANSISTORS

2.1. Introduction

Converting the native ligands on assemblies of colloidal nanocrystals has enabled their integration into solution-cast optoelectronic devices.[1,2] For instance, a versatile infrared absorber like PbSe NCs serve as active layers for prototypes of solution-processed field-effect transistors,[3-8] NC integrated circuits,[9] photovoltaic cells,[10-13] thermoelectric devices,[14] photodetectors,[15] and light-emitting diodes.[16] One of the most important challenges in amplifying their value as electronic materials lies in identifying appropriate surface ligands that facilitate stronger interparticle coupling and more efficient carrier transport within NC thin films.[17-19] Talapin and Murray demonstrated the dramatic impact of hydrazine treatment to coupled PbSe NCs in thin films to increase conductivity by ten orders of magnitude.[3] More recently, compact inorganic molecules such as chalcogenidometallate (ChaM) clusters,[4,14,20] metal-free chalcogenide ions,[21,22] and ammonium thiocyanate[23] have been successfully demonstrated as coupling agents to create conductive NC solids. These ligand chemistries, when applied in conjunction with newly developed processing methods and device architectures,[6,8,24,25] have enabled impressive electronic carrier mobilities in II-VI semiconductor NC films.[18] These advancements in the area of surface ligand

chemistries and device processing have created a promising opportunity for the incorporation of NC solids into emerging technological applications. In this study we introduce a processing method that uses the ChaMs to replace the insulating native oleic acid ligands in PbSe NCs.[27,28]

We investigate electronic transport in PbSe NC solids functionalized with the chalcogenidometallate clusters, or ChaMs (also known as metal chalcogenide complexes, or MCCs). ChaMs are hydrazinium-coordinated ions of metal chalcogenide semiconductors that readily bind to metallic atoms, and they can be restructured to form bulk material upon thermal treatment.[4,6,14,20,29-32] In previous reports, replacing the insulating ligand shells of semiconductor NCs with these clusters via solution exchange has demonstrated significant gains in electronic transport for CdSe NC field-effect transistors.[6,24] Using these methods, NC-ChaM composites have yielded impressive carrier mobilities (above 30 $cm^2V^{-1}s^{-1}$) for devices prepared with cadmium selenide and III-V semiconductor NCs.[24] Applying this surface chemistry to infrared absorbers like lead chalcogenides, for instance, may offer multiple advantages over conventionally used molecular linkers like hydrazine or 1,2-ethanedithiol. However, some NC species like the lead chalcogenides are less stable in suspensions when their native ligands are displaced in solution, thus requiring the development of robust processing methods to ensure that the electrical properties of functionalized NC films are consistent during the application of novel surface chemistries.

PbSe NCs have garnered much attention for applications in thermoelectric,[14,33,34] photovoltaic,[10-13] and field-effect transistor devices.[3,5,25,35] Due to the large Bohr diameter of the exciton (46 nm), the electronic structure in PbSe NCs in strongly quantum confined and the lowest energy transitions in these materials can be tuned through the near and mid-infrared.[36] Additionally, assemblies of PbSe NCs treated with shorter ligands have exhibited high carrier mobilities and the unique ability to switch between unipolar (n-type or p-type) and ambipolar transport depending on the surface chemistry.[37-39] These advantages, however, are offset by these materials' susceptibility to oxidative damage,[40] their labile surface chemistry,[41,42] and their tendency to agglomerate at relatively low processing temperatures,[3,5] which limits the variety of ligand chemistries that can electronically couple proximate NCs in a film. Despite these challenges, being able to apply a new surface ligand chemistry to PbSe opens opportunities for extending its versatility in other device applications and diversifying particle-ligand combinations for lead salt nanocrystals. Although the ChaM chemistry was previously applied using solution exchange to PbS and PbTe NCs,[2,12] we determined that the same procedure cannot be applied consistently to PbSe NCs. Most effective ligand conversion strategies PbSe NCs have been constrained to post-assembly conversion methods, wherein films of oleic acid-capped PbSe NCs are submerged in solutions that replace the native ligands with compact molecules like short-chain dithiols.

Previous studies of ChaMs as surface ligands for NCs employed solution exchange to replace the long chain hydrocarbon capping groups.[4,29] However, PbSe NCs flocculate into microscopic agglomerates when the ligands are exchanged in solution,

preventing them from being deposited as uniform films. Exchange methods in the solid film allow the functionalization of lead chalcogenide NC surfaces while avoiding these adverse effects. Milliron and co-workers previously reported a solid-phase exchange method that replaces the oleic acid surfactants in PbSe NCs with ChaMs and preserves the NCs within an inorganic matrix after annealing.[43] The protocol introduced by Milliron *et* al.[43] introduced new options to apply the ChaM chemistry on solid assemblies of NCs, and is remarkable for introducing a high temperature process that preserves the NCs size-dependent properties. To achieve this, PbSe NCs were deposited on substrates that were submerged into the ethanolamine-solvated ChaM solutions and then annealed to collapse the clusters around the NCs.[43] However, PbSe NC films readily delaminate in amine-terminated solvents, which are used to coordinate the ChaMs. Additionally, the ChaMs are insoluble in polar solvents like acetonitrile or acetone that are used to apply surface ligands like EDT or ammonium thiocyanate. We found that films of the PbSe-ChaM composites fabricated using the Milliron protocol easily delaminated from the substrate, which poses issues for electronic device applications. Here, we introduce additional processing steps that allow large area films of NC-ChaM composites to be generated via solid exchange while simulating the electronic characteristics of a field-effect transistor.

We demonstrate a ligand conversion procedure that converts films of oleic acid-capped PbSe NCs into PbSe-ChaM composites during post-assembly exchange. By carefully applying our processing conditions, we achieve n-type PbSe NC solids with electron mobilities of 1.3 $cm^2V^{-1}s^{-1}$ when functionalized with SnSe ChaMs, and 0.44 $cm^2V^{-1}s^{-1}$ when functionalized with In_2Se_3 ChaMs. Although previous manuscripts

have shown I-V measurements for lead salt based ChaM nanocomposites,[12] our work represents the first transistor measurements for these materials where the current can be gate modulated and n-type electrical characteristic to be observed. During device assembly, two critical steps were developed to ensure consistent device fabrication: 1) the use of substrates treated with thiol terminated silanes, and 2) submerging the NC assemblies in dilute hydrazine prior to the ChaM exchange to prevent film delamination in amine-terminated substrates. Submerging the films in dilute solutions of hydrazine removes a small but sufficient amount of oleic acid that binds the NCs strongly to the thiolated substrates; this prevents the NCs from delaminating when submerged in amine-based solvents like ethanolamine or hydrazine. Additionally, excitonic signatures in the optical absorption spectra of the PbSe NCs are preserved even when submerged in ChaMs solvated in anhydrous hydrazine. Previous work with PbSe NC films submerged in pure anhydrous hydrazine have reported ripening and damage in PbSe NC films.[5] After annealing our composites, the NCs remain distinct within the inorganic matrix. We demonstrate the compatibility of these surface ligands with PbSe NCs and a robust ligand replacement strategy than can be applied to NCs in the solid phase. To our knowledge, this is the first solid exchange procedure to produce functional PbSe-ChaM nanocomposites with high carrier mobility (>1 cm^2/V-s) without the aid of device modifications such as in-filling with high capacitance oxides or surface doping with lead atoms. In light of these encouraging figures, applying these device modifications to our inorganic nanocomposites could present new methods to enhance the performance of lead chalcogenide NC based optoelectronic applications.

2.2 Experimental Section

Materials. Lead Oxide (PbO, 99.999%), oleic acid (OA, tech. grade, 90%), 1-octadecene (ODE, 90%), anhydrous hydrazine (98%), selenium shots (99.99%), elemental sulfur (purum, 99.5%), elemental tin (powder, 99%), Indium(III) selenide (lumps), hexamethyldisilazane (99%), (3-mercaptopropyl)-trimethoxysilane (95%), ethanolamine (99.5%), and anhydrous n-hexane, acetonitrile, toluene, methanol, ethanol, tetrachloroethylene, and dimethylsulfoxide were purchased from Sigma-Aldrich and used without further processing. Tri-*n*-octylphosphine (97%) and Di-i-butylphosphine (97%) were purchased from Strem Chemicals.

NC Synthesis. *PbSe* NCs were prepared by using a modified procedure adopted from the method reported by Colvin and co-workers.[46] Due to the air-sensitive surface chemistry of lead chalcogenide NCs, all synthesis, processing, and device fabrication was carried out under nitrogen. In a typical synthesis, a 50 mL three-neck flask was loaded with 892 mg of PbO, 3.2 g of oleic acid, and 15.5 g of 1-octadecene and heated to 120°C under vacuum with stirring for 1.5 hours until the solution was transparent and colorless. The lead oleate precursor was transferred into a septa-capped vial and purged for 1 hour at 150°C before transferring into a glovebox for the remainder of the synthesis. Lead oleate (3 mL) was introduced into a 20 mL vial and heated to 190°C for 15 minutes over a hot plate. In a separate vial, 750 μL of 1.25 M selenium in tri-n-octylphosphine was mixed thoroughly with 15 μL of Di-*i*-butylphosphine and loaded into a syringe. When the lead oleate solution reached injection temperature, the selenium precursor was swiftly injected into the vial. Injection temperatures and reaction times were varied between 160 C°and 200°C and 2 to 5 minutes, respectively,

to modulate the NC sample to the desired size. To quench the reaction, the vial was immediately submerged into a cold alcohol bath and injected with 3.5 mL anhydrous ethanol to arrest the NC annealing. The NCs were isolated from the crude solution by centrifugation and precipitated twice more with hexane/methanol and hexane/ethanol before being dried and redispersed into anhydrous hexane at a concentration of 20 mg/mL. The NC solution was passed through a 0.2 μm PTFE filter prior to device fabrication. A portion of the solution was isolated, dried, and redispersed with tetrachloroethylene to obtain optical absorption spectra.

Chalcogenidometallate Synthesis. $(N_2H_5)_4(Sn_2S_6)$, $(N_2H_4)_3(N_2H_5)_4Sn_2Se_6$, and $(N_2H_5)_2(In_2Se_4)$ were synthesized using previously reported protocols.[4,31,32] All syntheses and handling of the molecular complexes, unless otherwise noted, were carried out in a nitrogen glove box. To prepare the tin sulfide molecular complex, an 8 mL vial was loaded with 118.7 mg (1 mmol) of elemental tin, 96.19 mg (3 mmol) of elemental sulfur and 4 mL of anhydrous hydrazine, capped, and stirred until a clear and nearly colorless solution formed in approximately 24 h. For the tin selenide molecular complex, 118.7 mg (1 mmol) of elemental tin, 236.88 mg (3 mmol) of ground selenium shots, and 4 mL of anhydrous hydrazine were combined in an 8 mL vial and stirred until a clear yellow-orange solution formed. The indium selenide complex was prepared by combining 466 mg (1mmol) of indium(III) selenide, 78.96 mg (1mmol) ground selenium shots, and 4 mL of anhydrous hydrazine and stirring until a nearly colorless, transparent, and viscous solution forms. After synthesis, the solutions were passed through a 0.2 μm PTFE filter and diluted with anhydrous hydrazine to prepare 0.1 M solutions of the cluster compounds. Alternatively, the

ligand exchange procedure can be conducted with more benign solvents like ethanolamine and dimethylsulfoxide (DMSO) by drying under nitrogen flow and redissolving in in ethanolamine (for the tin complexes) or 5:3 mixtures of ethanolamine and DMSO (for the indium complex) at concentrations of 50 mg/mL.

Ligand Exchange. Glass, silicon, or silicon with a thermally grown oxide were primed in a 1M solution of 3-(mercaptopropyl)-trimethoxysilane (MPTMS) for 2-3 hours before rinsing twice with anhydrous ethanol. The self assembled monolayer of MPTMS was used to promote wetting of the substrate and to prevent delamination of the NC films during ligand exchange. As-synthesized NCs were spin-coated (3000 rpm, 15 seconds) onto a primed substrate. The PbSe NC film was then submerged in a 1M solution of anhydrous hydrazine in acetonitrile for a minimum of 6 hours. The films were then rinsed in anhydrous acetonitrile and left to dry under nitrogen for 30 minutes. Thicker films were deposited with two additional layers of PbSe NCs, each soaked in dilute hydrazine for 6 hours.

Ligand exchange was performed by immersing the substrates for 20 minutes in either 0.1 M ChaM in hydrazine or in the ethanolamine or ethanolamine-DMSO solution as described above. The films were then rinsed for 30 seconds in anhydrous hydrazine and in two baths of anhydrous acetonitrile for 1 minute each. When dried, the substrates are placed onto a hot plate and heated to 80 C for 5 minutes, and then to 200 C for 20 minutes to remove counterionic hydrazinium species and any excess chalcogen coordinated to the ChaM complexes.

2.3. Ligand exchange mechanism

To apply the ChaM ligand chemistry to PbSe NC solids, we developed a sequential post-assembly conversion procedure to replace the oleate ligands and to encapsulate the NCs in an annealed ChaM matrix without sintering the NCs. Solution exchange methods are incompatible with PbSe, as the NCs tend to agglomerate in solution even after brief solution exchange times. Key steps of the method are detailed in **Scheme 2.1**. We found it necessary to develop procedures to 1) ensure films did not delaminate from the substrate and 2) prevent the NCs from ripening in the presence of the ChaM solvents. When this exchange was executed through the method reported by Tangirala *et* al.[43] (*i.e.*, without the addition of a monolayer and without a treatment solvent like dilute hydrazine) we found that the films delaminate completely when soaked in the ChaM solutions. To prevent delamination, PbSe NC films were deposited on substrates functionalized with a thiol-capped silane self-assembled monolayer (3-mercaptopropyltrimethoxysilane, MPTMS) that acts as a binding layer. To prevent ChaM and solvent damage to the NC films we found it necessary to treat the films in dilute hydrazine before they are soaked into the ChaMs and annealed into an entirely inorganic solid. PbSe NCs readily dissolve in ethanolamine, and are damaged by ripening when dipped into solutions of ChaMs dissolved in anhydrous hydrazine. Additionally, alcohols have been reported to induce irreversible surface damage in PbSe NC films and were avoided during the rinsing of the treated films.[5,28,44] In our modified procedure the films were submerged in 1 M solutions of hydrazine in acetonitrile prior to ChaM exchange. Dilute solutions of hydrazine act as

an n-type dopant, and partially reduce the interparticle spacing in films of PbSe NCs by removing sufficient oleic acid to render the films immobile on the substrate. We also observed that treating the films in dilute hydrazine solutions beforehand can prevent the NCs from ripening when submerged in ChaMs solvated in anhydrous hydrazine. We attribute the success of this mechanism to the ability of dilute hydrazine to stabilize PbSe NC films on substrates. Moreover, all rinsing procedures were carried out with anhydrous acetonitrile after the native ligands were replaced with the ChaMs. Unlike alcohols, acetonitrile does not damage the surfaces of semiconductor NCs,[44] and readily solvates excess ChaM solutions from the NC films.

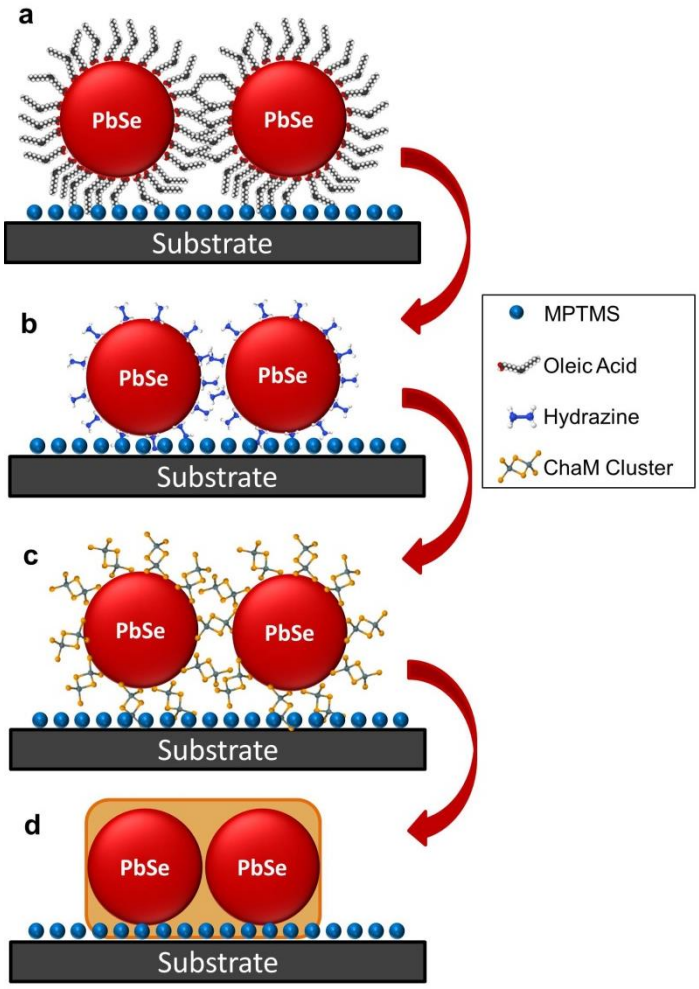

Scheme 2.1. Solid exchange procedure for functionalizing PbSe nanocrystal (NC) solids with ChaMs. (a) Films of oleic acid-capped PbSe NCs are soaked in (b) 1M hydrazine in acetonitrile before (c) replacing the ligands with ChaMs and (d) annealing at elevated temperatures to form an all-inorganic nanocomposite.

Developing ligand exchange procedures using solid assemblies of NCs requires careful attention to processing conditions to ensure a continuous, large-area film for device fabrication. NCs processed through solution exchange have the long insulating native ligands removed, and form a continuous assembly without need for further deposition.[4,23] For solid exchange procedures film voids are inevitable due to the reduction of film volume accompanying the displacement of surface bound ligands. Consequently, processing challenges like film delamination and solvent compatibility need to be considered. Priming substrates with thiol-capped silanes like (MPTMS SAM) during the preparation of solution-processed electronic materials,[35,45] binds the particles to the substrate. This is particularly important in the case of ChaM treatments to avoid dissolution or delamination of PbSe NCs from the substrate in solvents like pure anhydrous hydrazine and ethanolamine.

The use of SAMs to tether the NC to the substrate is insufficient to prevent delamination. We found that a pre-treatment solvent to strip a small fraction of the oleic acid surfactants must be employed in addition, to prevent the NCs from dissolving in the ChaM solutions. Conventional NC anti-solvents like methanol or ethanol can immobilize PbSe NC films onto a substrate, but their ability to strip off a large fraction of the native ligands and surface adatoms, to induce irreversible p-type behavior, and to suppress a transistor gate effect prompted our use of a milder stripping agent.[28,44] Instead of conventional anti-solvents, we found that dilute solutions of hydrazine as an optimal intermediate treatment in our ligand replacement strategy. We found that dilute solutions of hydrazine in acetonitrile produce highly conductive, n-type films of electronically coupled PbSe NCs.[3,5] The doping effects in

hydrazine-treated PbSe NC films are reversible, since n-type films can be rendered p-type by exposing them to oxygen or desorbing the hydrazine from the film under vacuum.[3] Dilute solutions of hydrazine in acetonitrile were also reported to quantitatively strip off < 7% of the original oleic acid from films of PbSe NCs,[5] which we determined to be sufficient in retaining films on the substrate when soaked in the ChaM solutions.

After treatment with dilute hydrazine, we submerged films in the ChaM cluster solutions. Since the anionic ChaMs are coordinated in molecular form by cationic hydrazine counterions, the positively charged metal atoms on the NC surfaces can coordinate with the inorganic clusters.[4] Thermal treatment removes excess chalcogen and hydrazinium ions and recrystallizes the ChaMs into an inorganic semiconductor matrix around the NCs. The films by compositions were determined to feature elements in both the PbSe NCs and the ChaMs. We focused our experiments in this study to using $SnSe_2$ and In_2Se_3 ChaMs, as these exhibited consistent gains in electrical transport for PbSe-ChaM composites.

2.4. Microscopic and Spectroscopic Evidence for Ligand Conversion

Transmission electron micrographs of the as-synthesized PbSe NCs deposited on a silicon nitride window have an average diameter of 8.3±0.4 nm (**Figure 2.1a,b**). After applying our ligand replacement procedure to the same silicon nitride window, the interparticle spacing is decreased while the average NC size remains essentially unchanged 8.8±0.4 nm and that the proximate particles are in intimate contact (Figure 2.1d,e). Scanning electron micrographs of these films illustrate a similar trend,

wherein films of as-synthesized PbSe NCs (Figure 2.1c) appear to pack into a less ordered and tighter cluster of NCs after ligand replacement (Figure 2.1f). Optical absorption spectra of the PbSe NC films show a first excitonic feature at 2180 nm for films with as-synthesized particles, which red-shifts to 2300 nm and broadens after ligand exchange but maintains the excitonic features **(Figure 2.2a)**. In combination, the absorption spectra and transmission electron micrographs confirm that our ChaM treated NCs do not sinter at the 200 °C treatment that is required to crystallize the ChaMs.

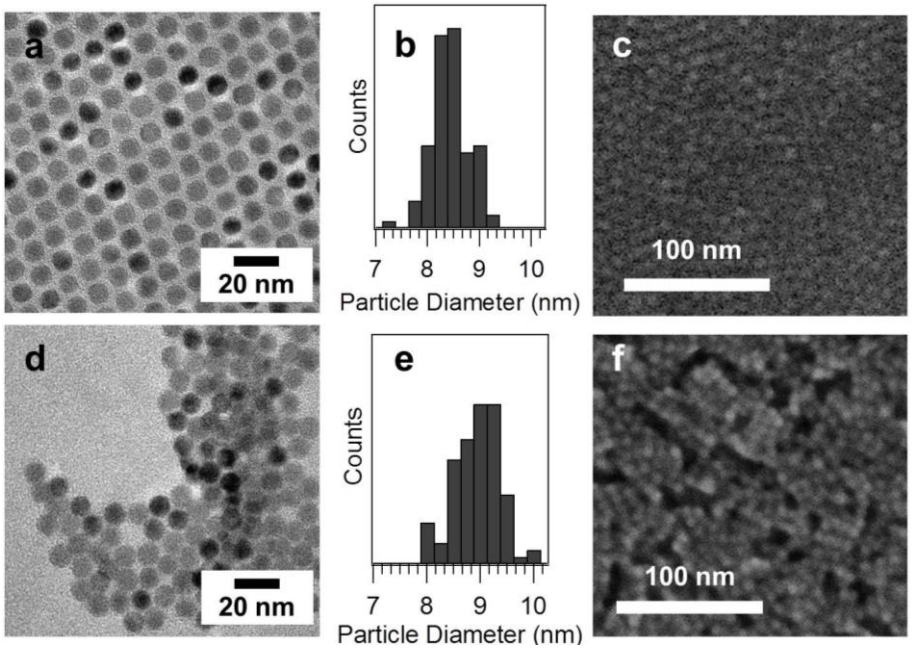

Figure 2.1. (a-c) Characterization of as-synthesized PbSe NCs: (a) TEM images of an array of as-synthesized 8.3±0.4 nm PbSe NCs capped with oleic acid ligands on a silicon nitride window.; (b) Size histogram of the PbSe NCs prior to ligand exchange.; (c) SEM image of a film of 8.3 nm as-synthesized PbSe NCs. (d-f) Characterization of NCs after solid exchange: (d) TEM image of the PbSe NCs of the same silicon nitride window as (a) after exchanging the oleic acid ligands with ChaMs via solid exchange. Average diameter of particles is 8.8±0.4 nm.; (e) Size histogram of the PbSe NCs after ligand exchange.; (f) SEM image of a film of 8.3 nm PbSe NCs treated with SnSe ChaMs using our solid exchange procedure.

Ligand replacement in the PbSe NC films can be monitored by comparing the transmission infrared spectrum of the sample during the exchange process. The vibrational fingerprints associated with the C-H stretches of oleic acid near 2900 cm^{-1} diminish upon immersion in dilute hydrazine solutions and disappear completely after the remaining oleate ligands are displaced by the clusters (Figure 2.2b). When the organic surfactants in CdSe NCs are replaced by the ChaMs in a solution exchange, the amount of ChaMs added must be quantitatively measured (equal to or below 10 mol% for CdSe-ChaM composites) to ensure a proper ratio of ChaM to NC surface area.[4] Excess ChaM has been reported to produce non-functional transistor devices,[4] since a dominant ChaM phase can divert charge transport from the NCs into the interparticle medium. X-ray diffraction of our functionalized PbSe NC films (**Figure 2.3**), however, show that the diffraction profile of PbSe NCs is retained even after ligand exchange and annealing, while no evidence of significant ChaM species is evident. These results indicate that the ChaM treatment of PbSe NCs was performed in proper proportion to create a ChaM matrix connecting the NCs.

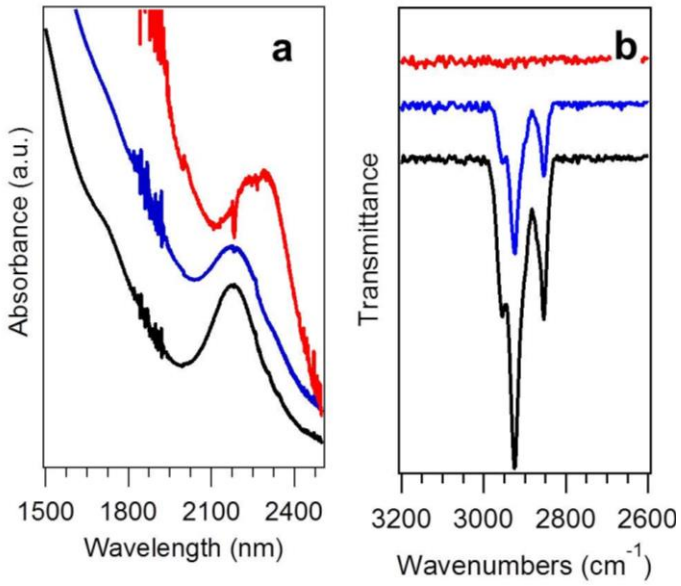

Figure 2.2. (a) Optical absorption spectra of oleic acid-capped PbSe NCs deposited as a film on a glass substrate (black) and treated in 1M hydrazine in acetonitrile (blue). After soaking the films in the ChaMs, the films are annealed at 200°C for 20 minutes (red). (b) Fourier-transform infrared transmission spectra of the same samples represented by the same color scheme in (a), depicting the suppression of C-H vibrational stretches associated with oleic acid as samples are subjected to ligand exchange.

2.5. X-Ray Analysis of PbSe-ChaM Nanocomposites

Scherrer peak width analysis of X-ray scattering patterns (Figure 2.3a) show the average crystallite size of assemblies with as-synthesized NCs to be 8.3 nm, and increases to 9.1 nm in the treated composites. The significant gains in thermal stability afforded by the presence of an inorganic matrix encompassing the NCs highlights one of the attractive features of this ligand chemistry, since PbSe NCs capped with oleic acid and short dithiol ligands like 1,2-ethanedithiol (EDT) readily sinter at temperatures as low as 80°C.[5] Similar conclusions regarding the preservation of crystallite size were confirmed by GISAXS (grazing incidence small angle x-ray scattering) patterns of a 6.4 nm PbSe superlattice assembly. When initially cast into a superlattice, the scattering patterns reveal a highly textured sample with well resolved in-plane and vertical packing and hexagonal ordering (Figure 2.3b). Following ligand exchange and annealing, the texture is reduced, but some hexagonal order remains (Figure 2.3c). A line projection along the q_x axis reveals the decrease in the average in-plane interparticle distance, with the initial superlattice film exhibiting an average spacing of 8.2 nm, corresponding to the added length of 1.8 nm associated with oleic acid ligands. After treatment, the composite features a d-spacing of 6.4 nm, which corresponds to the size of the original NC (Figure 2.3d). The GISAXS patterns from these materials suggest that regular interparticle spacing remains in the material after conversion, but reduced three-dimensional ordering.

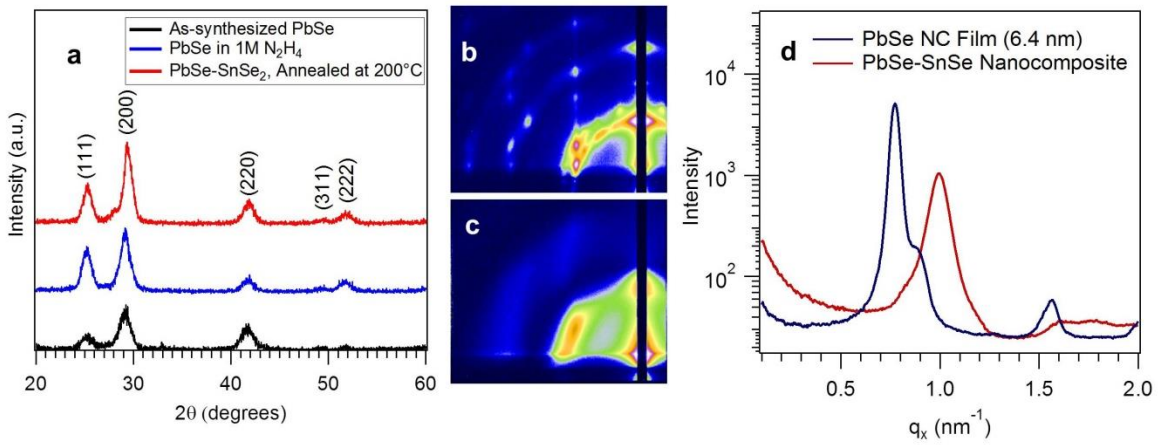

Figure 2.3. (a) X-Ray diffraction patterns of PbSe-$SnSe_2$ nanocomposite. The average crystallite size in films of PbSe NCs (black) is preserved when soaked in 1M hydrazine in acetonitrile (blue) and when organic surfactants are replaced with ChaMs and annealed (red). (b-c) Two-dimensional GISAXS patterns obtained from (b) 6.4 nm PbSe NC films cast into a superlattice assembly and (c) PbSe-$SnSe_2$ nanocomposite after annealing. (d) Intensity vs. q_x data taken from line cuts of the GISAXS pattern across the q_x axis.

2.6. Electrical Characterization of PbSe-ChaM Nanocomposites

Developing a reproducible solid exchange protocol for the ChaMs highlights the opportunity to apply this ligand chemistry to lead chalcogenide NC devices. For the PbSe NC solids, $SnSe_2$ and In_2Se_3 ChaMs were selected due to their previously reported transistor properties as independent ChaMs and in concert with CdSe NCs.[4,6,31,32] Our results demonstrate that higher conductivities and mobilities result from this ligand exchange **(Figure 2.4)**. The electron mobility of our PbSe NC-ChaM composites was calculated from the transfer characteristics of field-effect transistor (FET) measurements. For all electrical device experiments, 25-30 nm thick films of PbSe NCs capped with ChaM ligands were prepared by depositing NCs into the channel of lithographically patterned bottom-contact transistor devices and immersing them in ChaM solutions to replace the insulating ligands. A short annealing period at 180-200°C collapses the ChaMs and removes residual solvents and excess chalcogenide ions bound to the surface. Figures 2.4a,b shows sets of drain current (I_D) versus drain-source voltage (V_{DS}) scans at different gate voltages (V_G) for devices prepared with (a) $SnSe_2$-capped and (b) In_2Se_3-capped PbSe NCs. For both composites, n-type transport is observed. The transfer and output characteristics were reproducible under the following conditions: the PbSe NCs need to be synthesized, washed, and processed under a nitrogen atmosphere; only acetonitrile, ethanolamine, and hydrazine can be used as solvents for ligand exchange and processing; and the ligand exchange solutions containing the ChaMs have to be sufficiently dilute to prevent the conversion of our PbSe NC solid into a ChaM-dominant NC solid.

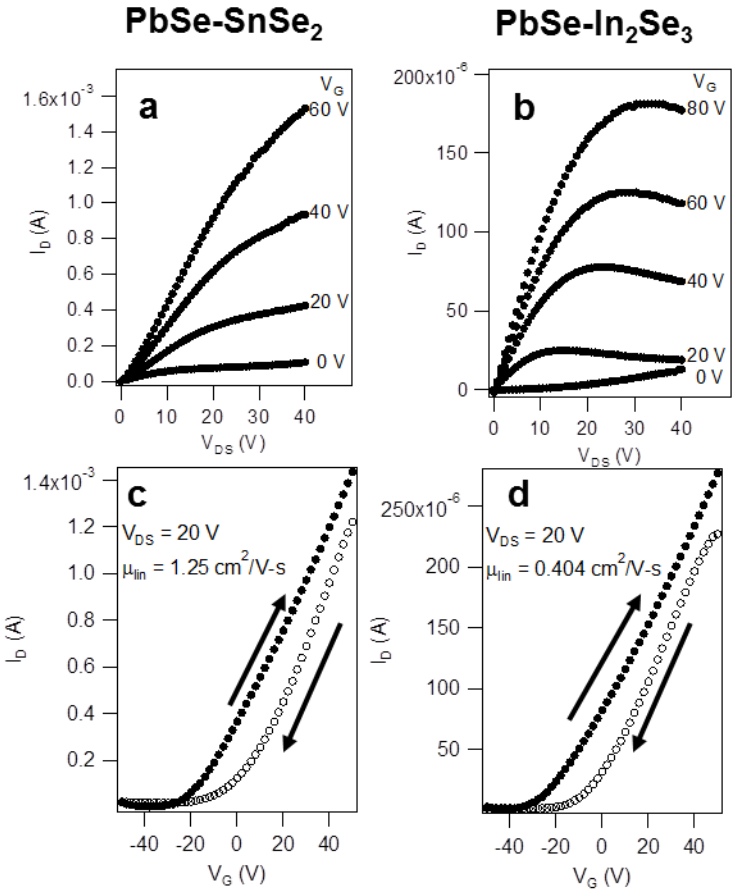

Figure 2.4. Charge transport characteristics of PbSe-ChaM composites (a-b) Drain current I_D vs. drain-source voltage V_{DS}, measured at varied gate voltages for field-effect transistors fabricated from PbSe NCs capped with (a)$SnSe_2$ and (b)In_2Se_3 ChaMs. (c-d) I_D-V_G plots at constant V_{DS}=40V used to determine linear regime field-effect mobility for devices capped with (c)$SnSe_2$ and (d)In_2Se_3 ChaMs. The devices exhibit n-type electrical transport, as displayed by increasing drain current corresponding with higher gate voltages. The higher mobility extracted for the PbSe-SnSe ChaM composite may be attributed to the lower temperatures required to crystallize SnSe vs. In_2Se_3.

We determined the electron mobility of our transistor devices by extrapolating the linear regime of FET operation (measured at V_{DS} = 40 V across a 50 μm long channel) in PbSe NC films capped with (c) $SnSe_2$ and (d) In_2Se_3 ChaMs. FETs assembled from PbSe-$SnSe_2$ ChaM composites annealed at 200°C show a μ_{lin} = 1.25 $cm^2V^{-1}s^{-1}$, which is two orders of magnitude higher than the best-performing PbSe NC devices treated with EDT,[19] and is within the range of mobility values that can be achieved by soaking the devices in hydrazine.[3,5] The saturation mobility calculated for the PbSe-$SnSe_2$ device is calculated to be μ_{sat} = 0.945 $cm^2V^{-1}s^{-1}$.For devices treated with In_2Se_3 ChaMs, the mobility extrapolated from the linear regime is μ_{lin} = 0.404 $cm^2V^{-1}s^{-1}$. Higher electron mobility for the tin selenide ChaM may attributed to the higher temperatures required to crystallize indium selenide.[31,32] For CdSe-based ChaM nanocomposites, NC solids treated with In_2Se_3 ChaMs have exhibited the highest electron mobilities of any ChaM species that associate with cadmium selenide NCs.[24] However, the CdSe-ChaM composites are annealed at temperatures of 250°C or higher to achieve these transfer characteristics. While CdSe-ChaM composites retain their nanocrystalline features at such conditions, these processing temperatures cannot be applied to PbSe-based composites, where excitonic features are eliminated above 220°C. However, at 200°C, the $SnSe_2$ ChaM is already crystalline whereas the In_2Se_3 ChaM remains amorphous, which may account for the higher mobility and conductivity observed in the tin-based composite devices. Other factors such as ionic diffusion between the ChaM species and the PbSe NCs may account for the changes in electronic character, and may occupy focus of a future study.

2.7. Conclusion:

New NC ligand exchange strategies that replace the insulating ligand shells with compact inorganic molecules are crucial for the development of NC-based optoelectronic devices. Due to their interesting optical and electrical properties, lead chalcogenide NCs have been extensively studied as active layer materials for several technological applications. However, the sensitive surface chemistry in these NCs limits all replacement procedures to post-assembly conversion of films. We demonstrate a solid exchange procedure for introducing the chalcogenidometallate clusters as capping ligands for PbSe NC solids. Our method details the beneficial effects of thiol-capped self-assembled monolayer to tether the NC to the substrate, a film-stabilizing treatment that uses dilute solutions of hydrazine in acetonitrile, and the use of gentle rinsing solvents like acetonitrile to fabricate PbSe NC devices treated with this chemistry. The ChaMs applied for these transistor devices yielded very conductive, high-mobility n-type FETs, with mobilities as high as 1.3 $cm^2V^{-1}s^{-1}$ for the PbSe-$SnSe_2$ composites. These cluster compounds expand the library of surface chemistries that can be applied towards lead chalcogenide nanostructures for electronic applications. Additionally, our work represents an alternative strategy for introducing new ligand chemistries to colloidal nanomaterials that cannot survive solution exchange during ligand replacement.

2.8. References

1. Murray, C. B.; Kagan, C. R.; Bawendi, M. G. *Annu Rev Mater Sci* **2000**, *30*, 545.
2. Kagan, C. R.; Murray, C. B.; Nirmal, M.; Bawendi, M. G. *Phys Rev Lett* **1996**, *76*, 1517.
3. Talapin, D. V.; Murray, C. B. *Science* **2005**, *310*, 86.
4. Kovalenko, M. V.; Scheele, M.; Talapin, D. V. *Science* **2009**, *324*, 1417.
5. Law, M.; Luther, J. M.; Song, O.; Hughes, B. K.; Perkins, C. L.; Nozik, A. J. *J Am Chem Soc* **2008**, *130*, 5974.
6. Lee, J. S.; Kovalenko, M. V.; Huang, J.; Chung, D. S.; Talapin, D. V. *Nat Nanotechnol* **2011**, *6*, 348.
7. Choi, J. H.; Fafarman, A. T.; Oh, S. J.; Ko, D. K.; Kim, D. K.; Diroll, B. T.; Muramoto, S.; Gillen, J. G.; Murray, C. B.; Kagan, C. R. *Nano Lett* **2012**, *12*, 2631.
8. Liu, Y.; Tolentino, J.; Gibbs, M.; Ihly, R.; Perkins, C. L.; Liu, Y.; Crawford, N.; Hemminger, J. C.; Law, M. *Nano Lett* **2013**, *13*, 1578.
9. Kim, D. K.; Lai, Y. M.; Diroll, B. T.; Murray, C. B.; Kagan, C. R. *Nat Commun* **2012**, *3*.
10. Choi, J. J.; Lim, Y. F.; Santiago-Berrios, M. B.; Oh, M.; Hyun, B. R.; Sung, L. F.; Bartnik, A. C.; Goedhart, A.; Malliaras, G. G.; Abruna, H. D.; Wise, F. W.; Hanrath, T. *Nano Lett* **2009**, *9*, 3749.
11. Ma, W. L.; Swisher, S. L.; Ewers, T.; Engel, J.; Ferry, V. E.; Atwater, H. A.; Alivisatos, A. P. *Acs Nano* **2011**, *5*, 8140.
12. McDonald, S. A.; Konstantatos, G.; Zhang, S. G.; Cyr, P. W.; Klem, E. J. D.; Levina, L.; Sargent, E. H. *Nat Mater* **2005**, *4*, 138.
13. Tang, J.; Kemp, K. W.; Hoogland, S.; Jeong, K. S.; Liu, H.; Levina, L.; Furukawa, M.; Wang, X. H.; Debnath, R.; Cha, D. K.; Chou, K. W.; Fischer, A.; Amassian, A.; Asbury, J. B.; Sargent, E. H. *Nat Mater* **2011**, *10*, 765.
14. Kovalenko, M. V.; Spokoyny, B.; Lee, J. S.; Scheele, M.; Weber, A.; Perera, S.; Landry, D.; Talapin, D. V. *J Am Chem Soc* **2010**, *132*, 6686.
15. Oertel, D. C.; Bawendi, M. G.; Arango, A. C.; Bulovic, V. *Appl Phys Lett* **2005**, *87*.
16. Sun, L. F.; Choi, J. J.; Stachnik, D.; Bartnik, A. C.; Hyun, B. R.; Malliaras, G. G.; Hanrath, T.; Wise, F. W. *Nat Nanotechnol* **2012**, *7*, 369.
17. Luther, J. M.; Law, M.; Song, Q.; Perkins, C. L.; Beard, M. C.; Nozik, A. J. *Acs Nano* **2008**, *2*, 271.
18. Talapin, D. V.; Lee, J. S.; Kovalenko, M. V.; Shevchenko, E. V. *Chem Rev* **2010**, *110*, 389.

19. Liu, Y.; Gibbs, M.; Puthussery, J.; Gaik, S.; Ihly, R.; Hillhouse, H. W.; Law, M. *Nano Lett* **2010**, *10*, 1960.
20. Kovalenko, M. V.; Bodnarchuk, M. I.; Zaumseil, J.; Lee, J. S.; Talapin, D. V. *J Am Chem Soc* **2010**, *132*, 10085.
21. Nag, A.; Kovalenko, M. V.; Lee, J. S.; Liu, W. Y.; Spokoyny, B.; Talapin, D. V. *J Am Chem Soc* **2011**, *133*, 10612.
22. Zhang, H. T.; Hu, B.; Sun, L. F.; Hovden, R.; Wise, F. W.; Muller, D. A.; Robinson, R. D. *Nano Lett* **2011**, *11*, 5356.
23. Fafarman, A. T.; Koh, W. K.; Diroll, B. T.; Kim, D. K.; Ko, D. K.; Oh, S. J.; Ye, X. C.; Doan-Nguyen, V.; Crump, M. R.; Reifsnyder, D. C.; Murray, C. B.; Kagan, C. R. *J Am Chem Soc* **2011**, *133*, 15753.
24. Chung, D. S.; Lee, J. S.; Huang, J.; Nag, A.; Ithurria, S.; Talapin, D. V. *Nano Lett* **2012**, *12*, 1813.
25. Oh, S. J.; Berry, N. E.; Choi, J. H.; Gaulding, E. A.; Paik, T.; Hong, S. H.; Murray, C. B.; Kagan, C. R. *Acs Nano* **2013**, *7*, 2413.
26. Stolle, C. J.; Panthani, M. G.; Harvey, T. B.; Akhavan, V. A.; Korgel, B. A. *Acs Appl Mater Inter* **2012**, *4*, 2757.
27. Dong, A. G.; Ye, X. C.; Chen, J.; Kang, Y. J.; Gordon, T.; Kikkawa, J. M.; Murray, C. B. *J Am Chem Soc* **2011**, *133*, 998.
28. Rosen, E. L.; Buonsanti, R.; Llordes, A.; Sawvel, A. M.; Milliron, D. J.; Helms, B. A. *Angew Chem Int Edit* **2012**, *51*, 684.
29. Cordones, A. A.; Scheele, M.; Alivisatos, A. P.; Leone, S. R. *J Am Chem Soc* **2012**, *134*, 18366.
30. Bag, S.; Trikalitis, P. N.; Chupas, P. J.; Armatas, G. S.; Kanatzidis, M. G. *Science* **2007**, *317*, 490.
31. Mitzi, D. B.; Copel, M.; Chey, S. J. *Adv Mater* **2005**, *17*, 1285.
32. Mitzi, D. B.; Kosbar, L. L.; Murray, C. E.; Copel, M.; Afzali, A. *Nature* **2004**, *428*, 299.
33. Ibanez, M.; Zamani, R.; Gorsse, S.; Fan, J. D.; Ortega, S.; Cadavid, D.; Morante, J. R.; Arbiol, J.; Cabot, A. *Acs Nano* **2013**, *7*, 2573.
34. Wang, R. Y.; Feser, J. P.; Lee, J. S.; Talapin, D. V.; Segalman, R.; Majumdar, A. *Nano Lett* **2008**, *8*, 2283.
35. Osedach, T. P.; Zhao, N.; Andrew, T. L.; Brown, P. R.; Wanger, D. D.; Strasfeld, D. B.; Chang, L. Y.; Bawendi, M. G.; Bulovic, V. *Acs Nano* **2012**, *6*, 3121.
36. Kang, I.; Wise, F. W. *J Opt Soc Am B* **1997**, *14*, 1632.
37. Zarghami, M. H.; Liu, Y.; Gibbs, M.; Gebremichael, E.; Webster, C.; Law, M. *Acs Nano* **2010**, *4*, 2475.
38. Kang, M. S.; Lee, J.; Norris, D. J.; Frisbie, C. D. *Nano Lett* **2009**, *9*, 3848.

39. Wehrenberg, B. L.; Yu, D.; Ma, J. S.; Guyot-Sionnest, P. *J Phys Chem B* **2005**, *109*, 20192.
40. Sykora, M.; Koposov, A. Y.; McGuire, J. A.; Schulze, R. K.; Tretiak, O.; Pietryga, J. M.; Klimov, V. I. *Acs Nano* **2010**, *4*, 2021.
41. Pietryga, J. M.; Werder, D. J.; Williams, D. J.; Casson, J. L.; Schaller, R. D.; Klimov, V. I.; Hollingsworth, J. A. *J Am Chem Soc* **2008**, *130*, 4879.
42. Moreels, I.; Fritzinger, B.; Martins, J. C.; Hens, Z. *J Am Chem Soc* **2008**, *130*, 15081.
43. Tangirala, R.; Baker, J. L.; Alivisatos, A. P.; Milliron, D. J. *Angew Chem Int Edit* **2010**, *49*, 2878.
44. Hassinen, A.; Moreels, I.; De Nolf, K.; Smet, P. F.; Martins, J. C.; Hens, Z. *J Am Chem Soc* **2012**, *134*, 20705.
45. Koh, W. K.; Saudari, S. R.; Fafarman, A. T.; Kagan, C. R.; Murray, C. B. *Nano Lett* **2011**, *11*, 4764.
46. Yu, W. W.; Falkner, J. C.; Shih, B. S.; Colvin, V. L. *Chem Mater* **2004**, *16*, 3318.
47. Kang, M. S.; Sahu, A.; Norris, D. J.; Frisbie, C. D. *Nano Lett* **2011**, *11*, 3887.

CHAPTER THREE

OPTICAL AND STRUCTURAL CHARACTERIZATION OF SOLVENT-VAPOR ANNEALED COLLOIDAL CADMIUM CHALCOGENIDE NANOROD FILMS STUDIED BY IN-SITU GISAXS

3.1 Introduction

Colloidal nanocrystals (NCs) represent a class of nanoscale materials that exhibit unique chemical and physical properties that are inaccessible in their bulk analogues.[1,2] Chemical synthetic methods have not only enabled the design of materials with a range of tunable sizes and morphologies, but also the tailoring of its chemical composition and structure.[3] When NCs are organized into an ensemble, the coupling between these building blocks may be exploited to design new functional materials that feature the quantum confined properties gained from constraining a material at the nanoscale spread over the dimensions of a thin film.[4] Some variations of these artificial solids have been into ordered single-component, binary, or ternary superlattices using isotropic NCs with specific compositions and size ratios.[5-8] Apart from the remarkable structural diversity that emerges from different combinations of NCs,[9] superlattice ordering may uncover new or enhanced functionalities for applications in optoelectronics, catalysis, or energy conversion.[10-14] Methods that facilitate the self-assembly of such superstructures have harnessed the coupling forces that drive NCs to reorganize between the interface of its liquid medium and either another immiscible liquid or a gas.[15-18] Understanding the mechanisms that enable the self-assembly of these materials enhances our ability to design new functional

materials with NCs as artificial atoms and to tailor these solids' properties based on composition and structure.[14]

While much of the previous work in NC superlattice self-assembly focused on structuring spherical NCs,[19] creating periodic structures with anisotropic materials has proven more challenging. Unlike spherical NCs, which tend to close-pack, anisotropic materials tend to exhibit unusual assembly properties by virtue of their geometry.[20] Part of the challenge in packing anisotropic crystals like rods,[21-24] tetrapods,[25-27] octapods,[28,29] platelets,[30] and other non-spherical NCs lies in the geometric contributions to self-assembly—the interparticle forces that facilitate close-packing in spherical materials do not apply to the mixed dimensions of the anisotropic crystal's volume, requiring alternative assembly techniques to achieve crystalline order.[31,32] Another factor that has hindered superlattice formation with anisotropic NCs is the quality and the monodispersity of the material suspensions.[33,34] While highly monodisperse isotropic materials were accessible during the initial stages of self-assembly experimentation, only more recently have synthetic methods yielded, for instance, cadmium chalcogenide nanorods (NRs) that feature very uniform aspect ratios.[35] The availability of high quality anisotropic building blocks hence allows a greater range of NC shapes to be cast into unique superlattice assemblies.[28,29,36,37] Due to their morphological anisotropy, alternative methods that go beyond colloidal crystalization in the self-assembly of these materials also merits further exploration.[38]

Cadmium chalcogenide NCs were among the first colloidal nanomaterials that demonstrated the ability to assemble into functional ordered superstructures.[5,39] When assembled into 3D superlattices, spherical CdSe NCs exhibited enhanced electronic

coupling and photoluminescence (PL) spectra with emission intensities correlated with assembly order.[40] When this material volume is extended from slightly prolate spheres to NRs, the material features new properties attributed to its anisotropy, such as a transition from nonpolarized to linearly polarized emission, length-dependent Stoke shifts, and longer carrier relaxation.[41] If the material were synthesized as a heterostructure, as with rods that encapsulate 0D CdSe spheres in a 1D CdS rod, its PL quantum yield enhancement, dimension-dependent excitonic delocalization, and the presence of both a rod and sphere based absorption band impart the material with more interesting optical and electronic properties.[35] Apart from introducing these geometry-dependent physical properties, the chemistry of cadmium chalcogenide NRs allows these building blocks to be atomistically designed into complex heterostructures. For instance, these NRs can be tipped with NCs of noble metals like Pt or Au for applications in photocatalysis,[42,43] with ferromagnetic elements like Co to provide the NR semiconductor and magnet functionalities,[44,45] and with PbSe to create a hybrid semiconductor nanostructure. When subjected to cationic exchange, cadmium chalcogenide NRs readily form other metal chalcogenide materials with 1D geometries inaccessible via conventional synthesis,[46-48] or striated NRs that contain a superlattice within a single nanostructure.[49-51] Ordered superlattices that use these semiconductor NRs as building blocks thus present an opportunity to design new functional artificial solids that can be integrated into applications such as photocatalysis, solar cells, and functional NR composites.[42,52-54]

Given their shape anisotropy, understanding mechanisms of self-assembly and the physical properties resulting from structural changes in 1D systems underscores an

important aspect in fabricating functional NR solids.[55,56] Previous methods that facilitate the self-assembly of NR superlattices have either employed long evaporation times in a controlled solvent environment or electric field-assisted assembly to promote vertical orientation.[21,57] Many of these studies focused on ex-situ microscopy imaging to monitor differences in assembly structure. [58,59] Although microscopy provides direct evidence of superlattice formation over localized areas, a method employed to study assembly formation uses small angle x-ray scattering (SAXS) techniques to monitor ordering in NC assemblies.[60,61] Scattering patterns obtained using SAXS provide information on the translational order in arrays of NCs during self-assembly. Even more powerful methods involve grazing incidence diffraction, which can be achieved by obtaining scattering patterns from NC assemblies under synchrotron radiation.[62-64] Grazing incidence scattering patterns offer a rich variety of information to describe the self-assembly of nanocrystalline materials. For instance, one study from the Alivisatos group monitored the assembly properties of CdSe NRs using ex-situ wide angle x-ray scattering (GIWAXS), wherein experimental parameters like solvent medium, temperature, substrate roughness, and self-assembled monolayer chain length were adjusted to examine their influence on rod assembly.[65] GIWAXS patterns obtained from these experiments were used to establish the average orientation of the rods over a large area when the experimental parameters were adjusted. Another study by Vanmaekelbergh *et* al. have focused on monitoring the dynamic structuring of rods into vertically oriented superlattices on a liquid-liquid interface via in-situ grazing incidence small-angle x-ray scattering (GISAXS) and ex-situ time-resolved TEM imaging.[66] By simulating the self-assembly conditions that

allowed NRs to organize vertically in a liquid-liquid interface, correlations were established between sequential microscopy samples and scattering patterns that described hexagonal NR lattices under GISAXS. While both techniques provide valuable information regarding local and ensemble ordering of the rod structures, reports that combine both methods to describe the ordering of NR superlattices have yet to surface.

Here, we present a study describing the mechanisms of self-assembly in dot-in-rod CdSe/CdS NR films wherein structural evolution is controlled via solvent interstitial concentration. While evaporation in a controlled solvent environment is not a novel technique,[24] the long times (>2 days) required to promote self-assembly under ambient conditions renders this method less feasible for the high-throughput processing of NR solids. Placing NR films in a controlled solvent environment, which can either saturate the interstitial spaces within the NR lattice with solvent vapor or a heated gas, allows for the relatively fast (~25 minutes) and reversible tuning of the rod assembly into vertically ordered superstructures. Additionally, the structural evolution of our assemblies is monitored by in-situ GISAXS and GIWAXS to describe both the translational ordering of individual rods and the assembly texture. Given the rods' optical anisotropy, we also obtained in-situ optical absorption measurements to investigate correlations between rod orientation and absorbance. The orientation dependence observed in our measurements were confirmed experimentally by polarization angle-adjusted PL emission spectroscopy and theoretically by determining the optimal angle of absorption and emission based on NC geometry. Based on our observations from grazing incidence diffraction and optical

spectroscopy, all three measurements collaboratively show that the oscillator strength is predominantly along the rod axes, and that the tunable alignment of the rods in our sample establishes optical anisotropy in a macroscopic scale. The reversibility of superstructure ordering demonstrated by this study presents a robust method that can be applied towards preparing high-throughput solid assemblies of anisotropic nanostructures. Additionally, the ability to monitor physical properties during structural evolution presents a new approach towards correlating structure with the in-situ optimization of functional NC solids.

3.2. Experimental Section

Materials. Cadmium oxide (CdO, 99.99%), propylphosphonic acid (PPA, 95%), tri-n-octylphosphine oxide(TOPO, 99%), toluene (ACS Reagent, 95%), 1,2-dichlorobenzene (99 %), elemental selenium (pellets, 99.99% trace metals basis), elemental sulfur (99%) , and anhydrous n-hexane, acetonitrile, toluene, methanol, and ethanol were purchased from Sigma-Aldrich and used without further processing. Tri-n-octylphosphine (97%) was purchased from Strem Chemicals. n-Octadecylphosphonic acid was purchased from Polycarbon Industries

NR Synthesis. *CdSe/CdS NRs.* Dot-in-rod CdSe/CdS nanostructures were synthesized by modifying the seeded synthesis approach presented by Carbone *et* al.[35] For the synthesis of the CdSe seeds, a 25 mL three-neck flask was loaded with 60 mg of CdO, 280 mg of ODPA, and 3.3 g of TOPO and heated to 150°C under vacuum with stirring for 2 hours. 1.7 M TOP:Se was prepared by mixing with a magnetic stirbar 3.60 g

TOP and 580 mg selenium pellets in a vial under nitrogen. After the cadmium phosphonate precursor was exposed to sufficient vacuum, the flask is heated to 370°C until the contents were optically clear. A 1.5 g quantity of TOP was then injected into the flask, and the contents were allowed to return to an injection temperature of 370°C. To grow 3.9 nm CdSe seeds, 450 μL of 1.7 M TOP:Se was swiftly injected into the flask. The temperature controller was immediately set to 350°C, and the flask was maintained at this temperature for 3 minutes. Upon reaching the desired size, the heating mantle was disengaged from the flask, and the solution was quenched by introducing 10 mL of room temperature anhydrous toluene when the solution reached 160°C and submerging the flask into an ice bath. The CdSe NCs were washed by two cycles of precipitation and redissolution in equal volumes of methanol and toluene. After a third precipitation in methanol, the seeds were dried under nitrogen and stored in a glove box. Prior to the synthesis of the seeded rods, a stock solution of equimolar TOP:S was prepared by combining 15 g of TOP with 1.2 g of elemental sulfur in a vial with stirring and heat (100°C) overnight. To prepare the seeded heterostructures, a 50 mL three-neck flask was loaded with 60 mg of CdO, 290 mg of ODPA, 60 mg of PPA, and 3 g of TOPO and heated to 150°C under vacuum with stirring for 2 hours. After sufficient vacuum, the flask was heated to 350°C until the precursor became optically clear. At this point, 1.5 g of TOP was injected into the flask, and the contents were allowed to return to the injection temperature of 350°C. The seed solution was prepared by sonicating the previously synthesized and dried CdSe NCs with TOP so that the solution reached a concentration of 400 μM. 200 μL of the TOP-solvated CdSe NCs are mixed with 1.62 g of the equimolar TOP:S. When the injection

temperature stabilized, this TOP:S mixture was injected into the flask, and the rods were allowed to grow for 8 minutes. The heating mantle was then disengaged from the flask, and the solution was quenched by introducing 10 mL of room temperature anhydrous toluene when the solution reached 160°C and submerging the flask into an ice bath. The NRs were washed by two cycles of precipitation and redissolution in equal volumes of methanol and toluene, and redispersed to a solution concentration of 5 mg/mL.

Grazing-incidence Scattering. Grazing incidence small angle X-ray scattering (GISAXS) measurements were performed on beam line D1 of the Cornell High Energy Synchrotron Source (CHESS) using monochromatic radiation of wavelength λ = 1.117 Å with a bandwidth Jλ/λ of 1.5%. The X-ray beam was produced by a hardbent dipole magnet of the Cornell storage ring and monochromatized with Mo:B4C synthetic multilayers with a period of 30 Å. The D1 area detector (MedOptics) is a fiber-coupled CCD camera with a pixel size of 46.9 μm by 46.9 μm and a total of 1024 × 1024 pixels with a 14-bit dynamical range per pixel. Typical read-out time per image was below 5 s. The images were dark current corrected, distortion-corrected, and flat-field corrected by the acquisition software. The sample to detector distance was 946 mm, as determined using a silver behenate powder standard. The incident angle of the X-ray beam was

varied from 0.25 to 0.5° i.e., slightly above the silicon critical angle. Typical exposure times ranged from 0.1 to 1.0 s. Scattering images were calibrated and integrated using the Fit2D software. GISAXS diffraction peaks were indexed and fitted using in-house software.2

After well-ordered GISAXS images were obtained, GIWAXS patterns on the same sample spot were recorded on Fuji image plates, and scanned for digital processing with a GE Healthcare Typhoon FLA-7000 image plate reader. Image plates were letter sized with 2000 x 2500 pixels and a 100 μm pixel size. For typical exposures of 2s an image plate was placed in a holder at 180 mm from the sample; the holder could be quickly slided in and out of scattering position on a rail. The intense scattering close to the direct beam was blocked with lead tape. Digital images were also analyzed using Fit2D.

For in-situ GISAXS/GIWAXS measurements, we used a custom-made vapor chamber with an aperture cut through the sample stage to enable the transmission of light for optical absorbance spectroscopy. A colloidal NR film deposited on an optically transparent substrate is positioned on the sample stage. The top of the stage was sealed, and a spectrometer was positioned on the cover to obtain optical transmission measurements. X-ray beams passed the chamber through Kapton windows. The sample is located on an elevated block and liquid solvent can be injected into the chamber through a long Teflon capillary from outside the hutch. A flow system delivered N_2 gas to modulate solvent vapor concentration inside the chamber. GISAXS peaks were indexed and fitted using our in-house software. A critical angle of 0.17 degree was found to give the best fit with our NR samples.

In-situ Optical Transmission. Optical transmission spectra of the NR arrays were simultaneously captured with scattering patterns during the assembly process. Optical spectra were obtained using a Filmetrics F30 Transmission Spectrometer fitted to the roof of the cell. The incident light was generated by a Navitar microscope white light

source with an adjustable halogen lamp. The light was introduced into the chamber by reflection using an angled mirror.

3.3. Self-assembly of Colloidal Nanorods via Solvent Vapor Annealing

The morphology and anisotropic physical properties of colloidal NRs provide an ideal model system for studying nanocrystal solids prepared with one-dimensional nanostructures. Due to their 1D morphology, NR materials not only self-assemble differently from spheres, but also exhibit orientation dependent optical properties that can be optimized in relation to its significantly longer c-axis. These NRs'anistropic character and their ability to confer nanocrystal assembly's properties by controlling its structural orientation offers an opportunity to correlate variations in ensemble structure with ensemble functionality. For our assembly experiments, we chose to study CdSe/CdS "dot-in-rod" heterostructures synthesized using the seeded method reported by Carbone *et* al., which exploits the wurtzite crystallographic structure of cadmium chalcogenide materials by growing the long CdS shell off the CdSe NC seed's basal plane. This method enables control over the nanostructure morphology by adjusting parameters like temperature, CdSe core size and concentration, and precursor ratios to obtain rods with tunable and highly uniform aspect ratios. The resultant material is a highly emissive heterostructure featuring two absorption bands that are associated with each structural component. Apart from its unique absorption profile, these core/shell NRs also exhibit optical properties characteristic to anisotropic systems, such as linearly polarized emission and aspect ratio dependent stoke shifts. The demonstrated optical anisotropy of these materials, in addition to the synthetic

advances that enable them to be prepared reliably with uniform aspect ratios, made them excellent candidates for performing concerted structural and optical studies that investigated incremental changes in material orientation and superlattice assembly with optical absorption. For these experiments, all NR samples were synthesized using a single seed size (3.9 nm) to establish comparisons between structural assemblies prepared from rods of varying lengths. Figure 3.1 displays conventional and high resolution transmission electron microscopy (TEM) images of three different CdSe/CdS NR samples with differing lengths that were used in these experiments. The NR samples shown have average lengths of 32.4±1.8 nm, 35.3±1.8 nm, and 46.9±1.7 nm (Figure 3.1 a,b,c), and are each accompanied on the right frame with a high resolution TEM image depicting the core's position within the heterostructure (Figure 3.1 d,e,f). Since the size distribution along the rod axis is fairly narrow, hexagonally ordered superlattices of these NRs are able to stack beyond monolayer assemblies.

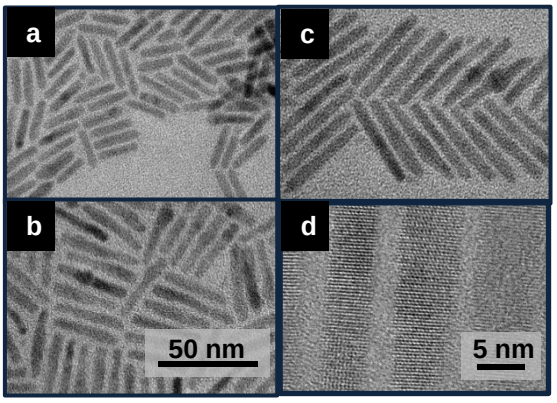

Figure 3.1. Colloidal semiconductor CdSe/CdS NR heterostructures that were used in self-assembled NR films. (a-c) Conventional TEM images of semiconductor NRs seeded with 3.9 nm CdSe nanocrystals. Each NR sample has a length of (a) 30 nm, (b) 35 nm, and (c) 45 nm. (d) HRTEM images of the 45 nm colloidal nanorods depicting the CdSe cores within the nanostructure, with the contrast between the lighter CdS nanorod and the CdSe dot depicting the differing structural components.

Preparing vertically oriented NR arrays can be carried out by adjusting parameters like NR dispersion concentration, solvent selection, evaporation temperature, and evaporation environment to promote the self-assembly of superlattice structures. One of the initially reported methods for preparing these arrays on solid substrates involved the controlled evaporation of CdS NRs dispersed in tetrachloroethylene or octane under the influence of heat and vacuum. Another more recently documented approach describes a self-assembly mechanism for CdSe/CdS heterostructure NRs, wherein NR dispersions in chlorobenzene are evaporated on substrates within a closed solvent vapor environment over several days to form multiple stacks of vertically oriented rod superlattices. However, these self-assembly methods either limit the formation of rod arrays over smaller surfaces (like TEM grids), or occur over very long time scales (generally over 24 hours), which may pose obstacles for the high throughput processing of functional NR assemblies. For our assembly experiments, we constructed a sealable vapor-solvent chamber with an elevated sample stage and a solvent trough to assist in the structural configuration of our NRs. Figure 3.2 depicts a schematic of our experimental setup, along with the characterization capabilities that we employed to study the structural and optical properties of our NR films. When the sealed chamber's trough is filled with solvent, the vapor molecules saturate the chamber and infiltrate the interparticle spaces occupied by organic surface ligands. When the ligands come into contact with solvent vapor, crystalline packing is suppressed, and the NRs disorder into a more liquid-like phase. The chamber is fitted with a gas inlet attached to a variable heating element, which functions to restructure the rods into ordered arrays via a heat-mediated

evaporation mechanism. This assembly approach thus combines the advantages demonstrated in previous methods through the inclusion of a heating element and high vapor pressure solvent environment to promote the orientation of rods into vertical arrays.

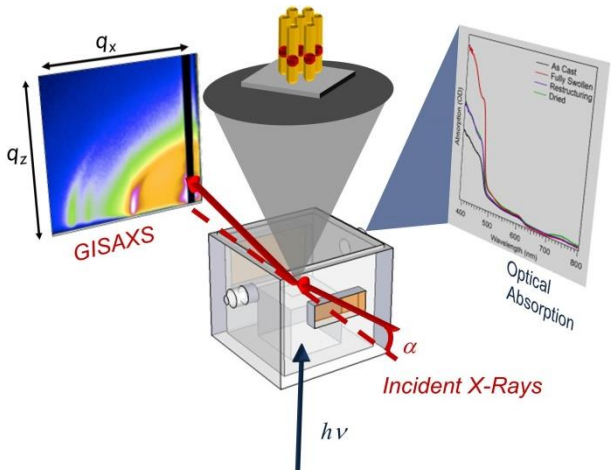

Figure 3.2. Representation of in-situ structural and optical characterization of colloidal nanorod assemblies. Nanorod orientational configuration is adjusting using a controlled solvent environment. Structural information is obtained via grazing incidence diffraction, while absorbance is probed using optical transmission.

The structural character of the self-assembled NR films are analyzed using grazing-incidence small-angle X-ray scattering (GISAXS) and grazing-incidence wide-angle X-ray scattering (GIWAXS) focused on the same sample spot. These grazing-incidence diffraction techniques provide extensive information regarding structure in NR arrays: GISAXS describes the translational ordering of individual rods as they

pack into a hexagonal superlattice, whereas GIWAXS reveals the average ensemble texture over the grains of NR superlattices. When films of NRs are placed within the chamber, grazing-incidence scattering patterns are collected in-situ during the vapor-saturation and evaporation processes to provide an overview of the self-assembly mechanisms that occur in NR arrays. In addition to probing structural character, the vapor-chamber was constructed with an optical path to obtain sequential optical transmission spectra using a custom-made spectrometer. Due to their anisotropic morphology, CdSe/CdS NRs exhibit orientation dependent optical properties that can be varied ex-situ either by changing the polarization angle using a polarizer, or in-situ by tuning the orientation of the rods on a substrate, the latter of which is achieved in the solvent chamber. Through this experimental setup, three different in-situ properties can be probed simultaneously to correlate assembly structure with optical characteristics.

For our assembly experiments, we initially form self-assembled films of the NRs by drop-casting a 30-50 μL quantity of a rod suspension in toluene (5 mg mL^{-1}) onto a 1 cm^2 cleaned glass slide and allowed the solvent to slowly evaporate under ambient conditions. In NR arrays, superlattice formation is ideally achieved by preparing monolayer or bilayer thick films of rods. In our experiments, in-situ optical properties were also probed in addition to grazing-incidence diffraction, which required thicker films to obtain sufficient optical absorption spectra. When the toluene had nearly evaporated, a 50 μL drop of 1,2-dichlorobenzene was dispersed over the surface of the NRs. The substrate was then placed into a saturated vapor environment with 1,2-dichlorobenzene vapor, and then allowed to evaporate slowly over 2 days to

form a vertically oriented assembly of NRs. These films are then placed into our constructed solvent chamber to demonstrate that the structural configuration of rods from vertical arrays to a disordered liquid crystalline phase is reversible and accompanied by changes in structural and optical character.

3.4. Grazing Incidence Diffraction Analysis of Nanorod Superlattices

We examined structural changes for five different NR samples with varying aspect ratios, and established that the self-assembly of the materials followed a similar pattern from sample to sample. Figure 3.3 shows grazing-incidence scattering patterns (GISAXS and GIWAXS) that correspond with the extreme (standing and disordered) configurations of our NR's structural assembly for a NR sample with an average length of 46.9 nm. The GISAXS pattern of a vertical NR array (Figure 3.3a) displays the first three orders of diffraction rings that are characteristic of a 2d hexagonal lattice, with the rings positioned at the radii q_1=0.9 nm^{-1}, q_2=1.5 nm^{-1}, and q_3=1.75 nm^{-1}. When these ratios between these radii are measured, they correspond with a q_1:q_2:q_3 = 1:√3:2 that correspond with hexagonal structures. When the rods disorder in the presence of solvent vapor, (Figure 3.3 b) the diffraction rings are completely suppressed, indicating the loss of hexagonal ordering. The GIWAXS patterns for these analogous structural configurations depict the same loss of vertical ordering in our NR arrays. Due to its crystallographic structure (wurzite), GIWAXS patterns of CdSe/CdS nanorods displays three diffraction rings that correspond with its one basal and two prism planes. Determining texture in NR arrays, in particular for one where standing rods dominate, is clearest from determining the angular width of the middle diffraction ring (basal plane). For an array of standing NRs, (Figure 3.3c) vertical orientation is

indicated by the pronounced texture of the basal plane. When the rods disorder, the diffraction ring becomes more diffuse and powderlike in character, which indicates a loss of texture. To initiate disorder, the solvent trough was filled with 2 mL of a 4:1 by volume mixture of toluene:1,2-dichlorobenzene. Upon exposure to solvent vapor, the initially ordered NR films disorder into a liquid phase, a process that happens over the course of 8-10 minutes. After the rod films are disordered, we introduce heated N_2 gas into the chamber to begin the evaporation of the NR films. The inlet gas line was affixed to a thermocouple, which indicated that the temperature at the end attached to the solvent chamber was maintained at a regular temperature of 80°C. When the heated gas is reintroduced into the chamber, the solvent takes approximately 10 minutes to evaporate from the interior into the outlet. During this period, a scattering pattern was captured with an integration time of 1 second every minute during film wetting and evaporation, and every 30 seconds when order begins to recover. Figure 3.3e,f shows a model of CdSe/CdS NRs corresponding with the extremes of the assembly's structural configuration. The scattering patterns and configurations depicted are reproducible for rod samples of differing aspect ratios.

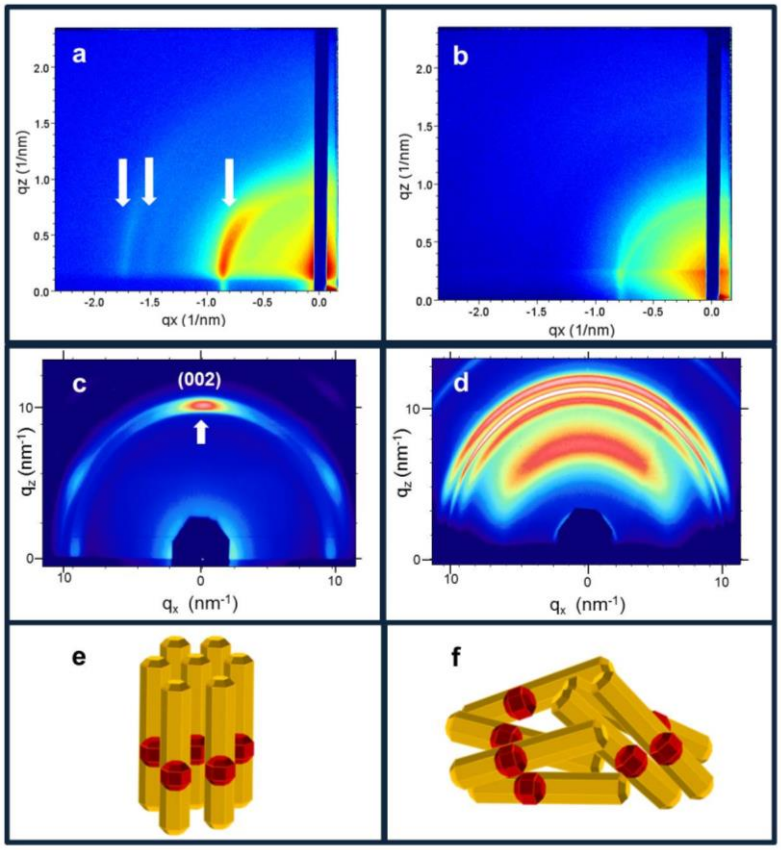

Figure 3.3. Grazing incidence scattering patterns that correspond with vertically oriented and disordered assemblies of 45 nm CdSe/CdS colloidal nanorods. The GISAXS pattern for a standing nanorod assembly (a) is characterized by the three reflections representative of a hexagonal lattice of cylinders, while the disordered assembly (b) exhibits none of this ordering. GIWAXS patterns for standing rods (c) are typified by the narrow angular width of the basal plane reflection. In a disordered nanorod assembly (d), this texture broadens and becomes more diffuse. Schematics (e,f) depicting both orientational extremes are included for reference.

GISAXS provides one of the most telling descriptions of self-assembly mechanisms for NR arrays by analyzing the diffraction rings characteristic of 2d hexagonal lattices. From the GISAXS pattern, the relative distances of the radii between the diffraction rings also provide lattice parameters to describe how lattice expansion and contraction occurs during the structural evolution. The value of conducting in-situ GISAXS experiments within our solvent chamber as we vary the structural configuration is highlighted by the changes in the intensities, the degree order of the diffraction rings and their lattice spacings. Figure 3.4 shows a sequence of four GISAXS patterns accompanied by line projections along the q_x direction that correspond to arrays of upstanding NRs, disordered NRs, NRs undergoing reconstruction, and restructured NRs. The initially cast film (Figure 3.4a) shows the first three order diffraction rings that correspond with the radii q_1=0.88 nm^{-1}, q_2=1.52 nm^{-1}, and q_3=1.74 nm^{-1}, and a lattice parameter of a=8.4 nm. The ratios of these radii correspond with the q_1:q_2:q_3=1:$\sqrt{3}$:2 distances in 2d hexagonal lattices, whereas the lattice parameter can be described by standing rods with a diameter of 5.6 nm separated from each other by two layers of ODPA ligands. The NR film is then exposed to solvent vapor, and disorder is achieved within ten minutes. The scattering intensity is not constant along the diffraction ring, which indicates that the structures are preferentially oriented in the vertical direction, but do not assume a perfectly standing configuration. When the rod film swells and disorders (Figure 3.4b), the diffraction rings are eliminated, and radial distance of the much more diffuse first diffraction ring expands to q_1=0.81 nm^{-1}. After the film completely disorders, heated inert gas (inlet temperature is at 80°C) is introduced into the chamber, and the NR

arrays begin recovering structure within 10-15 minutes. When structure begins to recover (Figure 3.4c), the diffraction rings of the 2d hexagonal lattice reappear with the addition of a fourth order peak, corresponding to a radius of q_4=2.15 nm^{-1}. The second diffraction ring does not feature any intensity in this scattering pattern, which is characteristic of films where the interstices still retain solvent molecules. The diffraction rings' radii in this GISAXS pattern corresponds with q_1=0.83 nm^{-1}, q_2=1.63 nm^{-1}, and q_4=2.15 nm^{-1} (ratio q_1:q_2:q_4=1:2:√7), and the lattice parameter for this NR array is a=9nm, which indicates that solvent molecules caused the lattice to expand during solvent vapor infiltration. Complete solvent evaporation occurred after 20 minutes of exposure to hot N_2 gas. When the solvent vapor is completely evacuated from the chamber (Figure 3.4d), we observe the emergence of all four diffraction rings, with the radii situated at with q_1=0.87 nm^{-1}, q_2=1.47 nm^{-1}, q_3=1.70 nm^{-1}, and q_4=2.24 nm^{-1}, with the ratios for these radii corresponding to q_1:q_2: q_3:q_4=1:√3:2:√7. The lattice parameter for this sample was calculated to be a=8.6 nm, indicating lattice expansion from the original film's lattice parameter of a=8.4 nm. The diffraction rings for the restructured NR arrays also exhibit a more diffuse scattering intensity compared with the original film, which indicates that while the rods have a preferential vertical orientation, the angle of the standing array is more randomly distributed along the x-z plane. All of these trends in structural evolution are represented by the line projections for our patterns along q_x (Figure 3.4e-h). For all of our other NR samples, we observed that from the initial upstanding arrays, lattice expansion occurs and the scattering intensity of the diffraction rings becomes less pronounced after disorder and restructuring. Since these films were cast as multilayers

in order to obtain sufficient in-situ optical transmission spectra, ideal NR superlattices could not be obtained within the time scales we were operating under to configure our materials' structure, which may be achievable through monolayer thick films of NRs. In our samples, we form stacks of ordered monolayers, but without any correlation between the layers. Nevertheless, the use of our solvent chamber technique demonstrated the reversibility of structural configuration and displayed the characteristic features of a standing hexagonal superlattice, and can be employed towards future investigations of superlattice assembly in thinner layers of NRs.

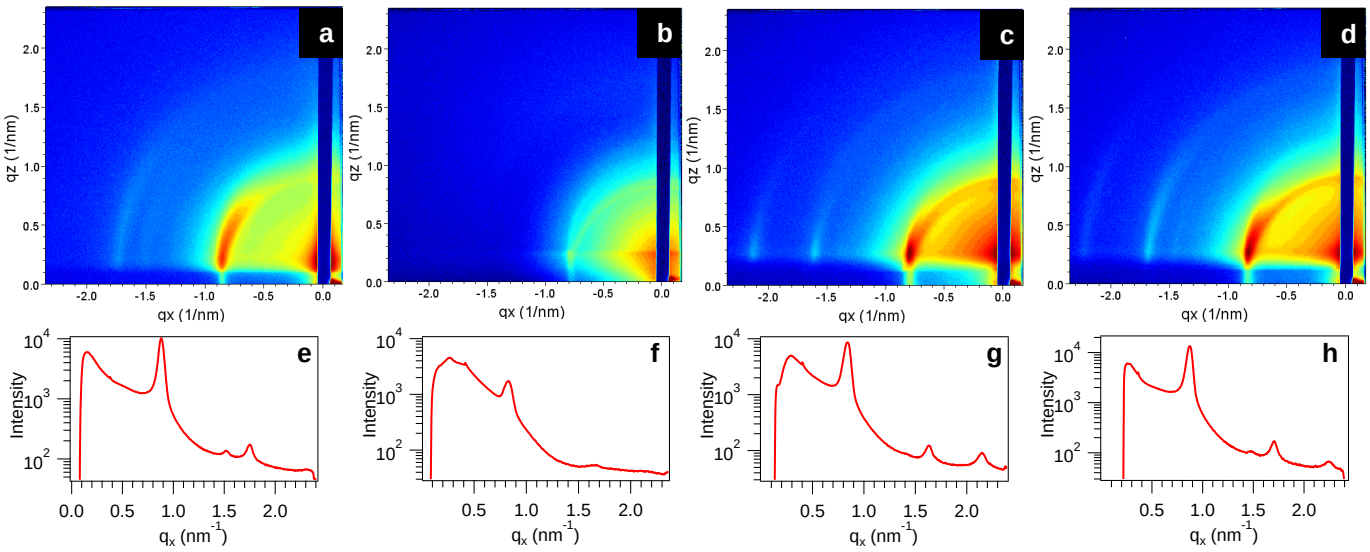

Figure 3.4. In-situ GISAXS patterns and line projections depicting the signature diffraction rings that correspond with a 2D hexagonal lattice of an array of 46.9 nm long CdSe/CdS NRs exposed to solvent vapor and redried. (a-d) GISAXS patterns that depict structural evolution of a 2D hexagonal superlattice of vertically oriented NRs. NR array is initially cast to form a standing NR superlattice (a), and exposed to solvent vapor to induce disorder (b). After a heated gas is introduced into the solvent chamber, the structure of the NR lattice gradually recovers (c), and exhibits higher order diffraction rings when dried (d). (e-h) Line projections along q_x capture the radial positions of the hexagonal superlattice's diffraction rings. The initial projection (e) exhibits the first three order peaks in a 2D hexagonal lattice, which are eliminated when the array disorders (f). When the NR array restructures (g), lower order diffraction peaks reemerge first, and the final projection depicts a NR superlattice with first, second, third, and fourth order diffraction peaks present.

Apart from superlattice character, grazing-incidence diffraction can also provide information about assembly texture when the area under investigation is greatly expanded. GIWAXS patterns for cadmium chalcogenide NRs, which crystallize in the anisotropic wurtzite structure, feature three characteristic diffraction rings—two of which correspond with its [100] and [101] prism planes, a middle ring that corresponds with its [002] basal plane. When NRs organize into an upstanding array, the intensity of the diffraction ring corresponding with the basal plane becomes pronounced, and the signal is confined within a narrow angular width at q_x=0. The narrower the intensity of the texture, the more preferentially oriented the NR array is in the vertical direction. Figure 3.5 shows GIWAXS patterns for different structural configurations of an NR assembly prepared with 46.9 nm building blocks, along with accompanying plots of the azimuthal integration along the direction χ which measures the angular width of the basal plane texture. GIWAXS patterns of the initially cast NR film (Figure 3.5a), which is prepared such that the rods are preferentially oriented in the vertical direction, shows a pronounced texture at q_x=0, which becomes more diffuse when disorder is introduced into the rods (Figure 3.5b). As structure recovers (Figure 3.5c) the basal plane texture becomes more pronounced, and the diffraction profile of standing rods is restored when the film is completely dry (Figure 3.5d). The azimuthal integration plots that accompany each GIWAXS pattern shows that the peak width of the basal plane texture is narrow when the film is initially cast (Figure 3.5e), becomes diffuse when the NR array disorders upon solvent exposure (Figure 3.5f), and recovers its peak after exposure to heated gas (Figure 3.5g,h). The distribution of upstanding rods in the NR array and their angle relative to the substrate can be

approximated by extrapolating the FWHM of the peak resulting from the integration along the azimuthal direction. Peak analysis indicates that the initially cast sample consists of upstanding rods that generally deviate 12.8º from a perfectly standing configuration, and upon recovery on average deviate 18.5º from a vertical orientation. These results corroborate our findings from GISAXS, which suggests that the pronounced scattering intensity of the diffraction ring in the initial samples becomes more diffuse upon structure recovery. Conducting GISAXS and GIWAXS in concert thus provide an opportunity to correlate changes in the materials' structural configuration with their translational ordering and texture.

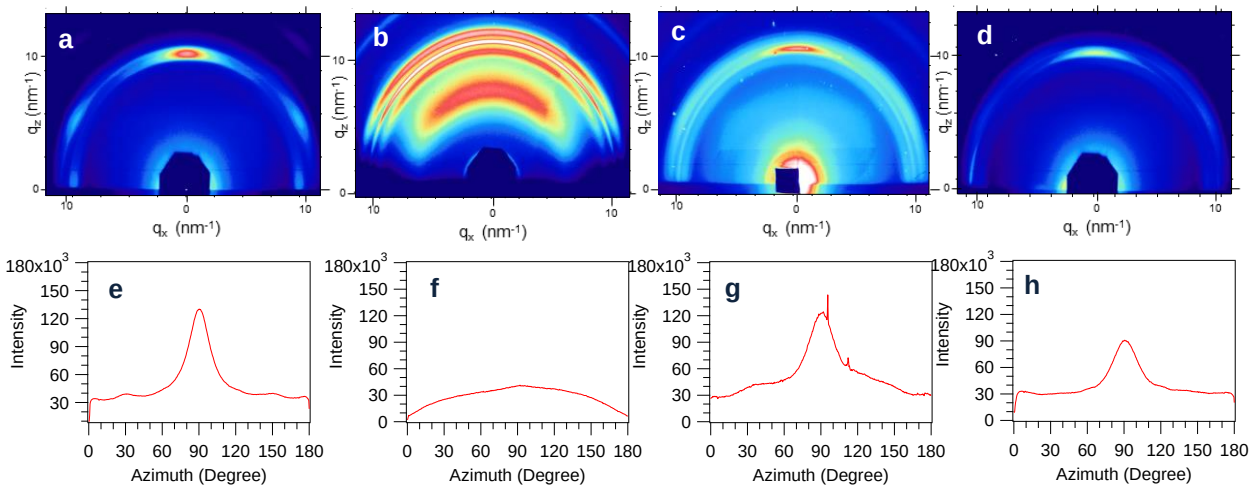

Figure 3.5. In-situ GIWAXS patterns and azimuthal integrations of the diffraction ring corresponding with the rod's basal plane [002] for an array of 46.9 nm long CdSe/CdS NRs exposed to solvent vapor and redried. (a-d) GIWAXS patterns that depict the evolution of texture during the orientation process in a NR array. Initially, the as cast NR array (a) shows a pronounced texture from the basal plane diffraction ring that becomes diffuse after disorder is introduced (b). This trend is reversed upon introduction of heated gas (c), and the pronounced texture is recovered after drying the NR array completely. (e-h) Integrating along the azimuthal directions approximates the angular width of the basal plane reflection, and illustrates how an initially narrow peak width broadens and recovers during solvent exposure and evaporation.

3.5. In-situ Optical Absorption Spectroscopy of Nanorod Assemblies

Due to these rods' optical anisotropy, we configured our experiment to investigate changes in optical transmission based on structural configuration. Figure 3.6 shows the experimental geometry and the spectra we obtained for 46.9 nm NR arrays at different structural configurations. Our solvent chamber was fitted with a fiber optic spectrometer setup to capture optical spectra in real time while scattering patterns were being obtained. The schematic for our optical transmission setup is shown in Figure 3.6a, where light from a variable fiber optic white light source is transmitted through the sample stage and through an optically transparent substrate. As the rods change orientation as a function of solvent vapor concentration according to our in-situ GISAXS patterns, we capture a corresponding optical spectrum to probe the effects of anisotropic absorption in tunable NR assemblies. Figure 3.6b describes a general trend that we observed for all NR assemblies, wherein an initially cast film of upstanding NRs exhibits the lowest absorptivity, whereas a disordered film shows a pronounced gain in optical absorbance. As the structure recovers, optical transmission also diminishes. The extreme configurations and the trends in absorption are described by Figure 3.6c. The light source used in our experiment was not polarized, but was directed such that the propagation of light was perpendicular to the substrate, creating a plane of randomly distributed polarization in the plane of the substrate. When the rods assume an upstanding configuration, polarization is perpendicular to the rod axes, which results in reduced absorption and thus increased transmission. Upon introducing disorder to its structural configuration, the rods are randomly distributed and oriented

parallel to the substrate, which coincides with the direction of random polarization, giving rise to more pronounced absorption, and reduced transmission.

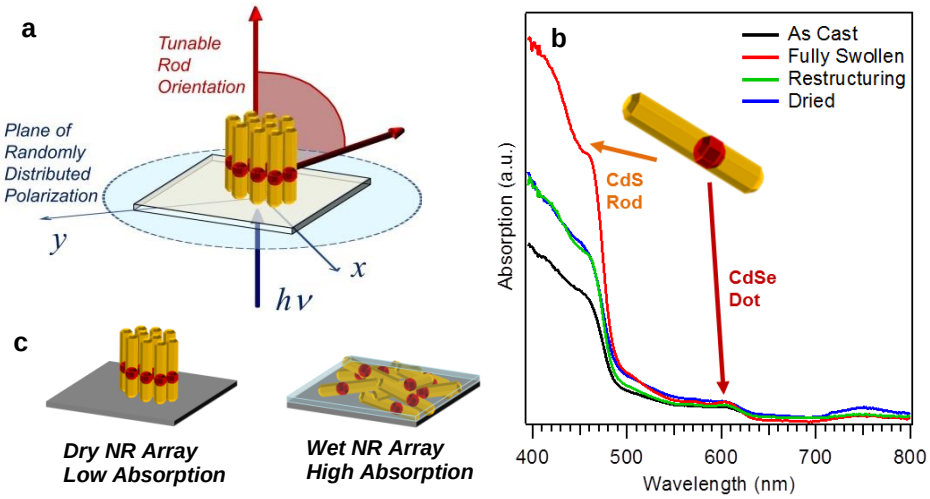

Figure 3.6. Experimental schematic and absorption spectra for in-situ optical experiments conducted in the synchrotron hutch. (a) Schematic depicting the experimental geometry used to probe NR absorption as rod orientation is varied by interstitial solvent concentration. (b) Absorption spectra for a NR array prepared with 46.9 nm long (AR: 9) rods corresponding with its different structural configurations. (c) Trends observed within the extremes of NR structural configuration.

3.6. Ex-situ Polarization-Dependent Photoluminescence

To verify that our observation of the orientation dependent absorption is not due to other extrinsic factors (such as change of dielectric constant of the environment, or aggregation of particles during the drying process), we obtained ex-situ polarization dependent photoluminescence measurement. Previous reports on optical properties of these NRs have shown that its photoluminescence (PL) emission is highly polarization dependent, with predominant polarization parallel to the rod axis. Figure 3.7a shows the schematic of the ex-situ setup. A 405nm diode laser was used as the excitation source, shining perpendicular to the substrate. A monochromator and a detector was placed 90 degrees to the excitation beam. A linear polarizer was placed between the sample and the detector to pick up a particular polarization for emission. A half wave-plate was placed between the polarizer and the detector to rotate the polarization to a fixed direction so that the grating and detector efficiency is kept constant.

Figure 3.7b shows the measured PL intensity as a function of the angle of the polarizer. 0 degree corresponds to p polarized light (perpendicular to the substrate), and 90 degree corresponds to s polarized light (parallel to the substrate). The result shows clear polarization dependence, with dominant light polarization perpendicular to the substrate, and therefore parallel to the aligned nanorods axis. The corresponding polarization ratio $(I_p - I_s)/(I_p + I_s)$ is 12.5%. The reduced polarization ratio compared with measurement on single rod particle is due to the imperfect alignment of rods.

To further confirm our results, we took the same sample, and reorder the nanorods by dropping hexane, and let it evaporate naturally. We used the same optical

setup, and polarization ratio was found to be -41.5%, with dominant light polarization parallel to the substrate.

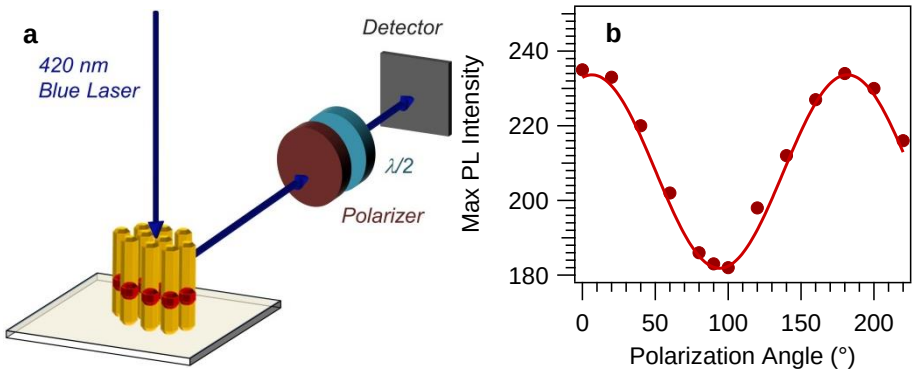

Figure 3.7. Schematics and optical spectra for ex-situ polarization dependent PL emission and absorption measurements. (a) Schematic depicting a polarization-dependent PL emission experiment for our NR array. (b) Maximum PL intensity as a function of polarization for an NR array of 46.9 nm rods.

3.7. Conclusion

NC superlattices prepared from anisotropic building blocks like NRs require alternative approaches to self-assembly to enable the design of functional NC solids with non-spherical geometries. Colloidal NRs have been demonstrated to exhibit different optical and electronic properties depending on the nanostructure's geometry. As such, the methods used to organize the materials in relation to the rod axis are crucial for defining the properties of the solid. To assemble the NRs using our method, we sealed a substrate cast with colloidal CdSe/CdS NRs within a chamber with an elevated stage. The NRs disordered when the chamber was saturated with the vapors of high boiling point organic solvent, and oriented vertically when a heated gas was introduced into the interior. Grazing incidence techniques were employed to establish material structure for the superlattice and the general orientation of the rods. GISAXS provided information regarding superlattice assembly during structural evolution, whereas GIWAXS described the relative orientation of the NRs on the substrate. In-situ optical transmission measurements carried out simultaneously show that absorption is most pronounced in a disordered NR sample where rods are most likely oriented parallel to the substrate, whereas it is most suppressed in a vertically oriented NR sample where the nanostructure is perpendicular to the substrate. Ex-situ optical experiments depict the polarization dependence of the NR assemblies, and support the in-situ measurements we performed using synchrotron radiation. Our method demonstrates an effective approach to correlating superlattice assembly order with changes in the physical characteristics of an NC solid. Further experiments using our method can explore different parameters and assembly times to achieve different

assembly patterns with NRs or other anisotropic building blocks. Additionally, modifications can be applied to our characterization method to study different physical characteristics such as in-situ electrical transport or photoconductivity measurements in other NR arrays.

3.8. References

(1) Alivisatos, A. P. *The Journal of Physical Chemistry* **1996**, *100*, 13226.

(2) Alivisatos, A. P. *Acs Nano* **2008**, *2*, 1514.

(3) Alivisatos, A. P. *Science* **1996**, *271*, 933.

(4) Murray, C. B.; Kagan, C. R.; Bawendi, M. G. *Annu Rev Mater Sci* **2000**, *30*, 545.

(5) Murray, C. B.; Kagan, C. R.; Bawendi, M. G. *Science* **1995**, *270*, 1335.

(6) Bodnarchuk, M. I.; Kovalenko, M. V.; Heiss, W.; Talapin, D. V. *J Am Chem Soc* **2010**, *132*, 11967.

(7) Shevchenko, E. V.; Talapin, D. V.; Kotov, N. A.; O'Brien, S.; Murray, C. B. *Nature* **2006**, *439*, 55.

(8) Dong, A. G.; Ye, X. C.; Chen, J.; Murray, C. B. *Nano Lett* **2011**, *11*, 1804.

(9) Shevchenko, E. V.; Talapin, D. V.; Kotov, N. A.; O'Brien, S.; Murray, C. B. *Nature* **2006**, *439*, 55.

(10) Chen, J.; Ye, X. C.; Oh, S. J.; Kikkawa, J. M.; Kagan, C. R.; Murray, C. B. *Acs Nano* **2013**, *7*, 1478.

(11) Dong, A. G.; Chen, J.; Ye, X. C.; Kikkawa, J. M.; Murray, C. B. *J Am Chem Soc* **2011**, *133*, 13296.

(12) Kang, Y.; Li, M.; Cai, Y.; Cargnello, M.; Diaz, R. E.; Gordon, T. R.; Wieder, N. L.; Adzic, R. R.; Gorte, R. J.; Stach, E. A.; Murray, C. B. *J Am Chem Soc* **2013**, *135*, 2741.

(13) Ahmed, S.; Ryan, K. M. *Chem Commun* **2009**, 6421.

(14) Urban, J. J.; Talapin, D. V.; Shevchenko, E. V.; Kagan, C. R.; Murray, C. B. *Nat Mater* **2007**, *6*, 115.

(15) Talapin, D. V.; Shevchenko, E. V.; Murray, C. B.; Titov, A. V.; Kral, P. *Nano Lett* **2007**, *7*, 1213.

(16) Bigioni, T. P.; Lin, X. M.; Nguyen, T. T.; Corwin, E. I.; Witten, T. A.; Jaeger, H. M. *Nat Mater* **2006**, *5*, 265.

(17) Dong, A. G.; Chen, J.; Vora, P. M.; Kikkawa, J. M.; Murray, C. B. *Nature* **2010**, *466*, 474.

(18) Bodnarchuk, M. I.; Erni, R.; Krumeich, F.; Kovalenko, M. V. *Nano Lett* **2013**, *13*, 1699.

(19) Korgel, B. A.; Fullam, S.; Connolly, S.; Fitzmaurice, D. *J Phys Chem B* **1998**, *102*, 8379.

(20) Onsager, L. *Ann Ny Acad Sci* **1949**, *51*, 627.

(21) Singh, A.; Gunning, R. D.; Ahmed, S.; Barrett, C. A.; English, N. J.; Garate, J. A.; Ryan, K. M. *J Mater Chem* **2012**, *22*, 1562.

(22) Singh, A.; Coughlan, C.; Laffir, F.; Ryan, K. M. *Acs Nano* **2012**, *6*, 6977.

(23) Singh, A.; Gunning, R. D.; Sanyal, A.; Ryan, K. M. *Chem Commun* **2010**, *46*, 7193.

(24) Zanella, M.; Gomes, R.; Povia, M.; Giannini, C.; Zhang, Y.; Riskin, A.; Van Bael, M.; Hens, Z.; Manna, L. *Adv Mater* **2011**, *23*, 2205.

(25) Franchini, I. R.; Cola, A.; Rizzo, A.; Mastria, R.; Persano, A.; Krahne, R.; Genovese, A.; Falqui, A.; Baranov, D.; Gigli, G.; Manna, L. *Nanoscale* **2010**, *2*, 2171.

(26) Chao, K. P.; Bagaria, H.; Wong, M. S.; Biswal, S. L. *J Colloid Interf Sci* **2012**, *378*, 58.

(27) Goodman, M. D.; Zhao, L.; DeRocher, K. A.; Wang, J.; Mallapragada, S. K.; Lin, Z. Q. *Acs Nano* **2010**, *4*, 2043.

(28) Miszta, K.; de Graaf, J.; Bertoni, G.; Dorfs, D.; Brescia, R.; Marras, S.; Ceseracciu, L.; Cingolani, R.; van Roij, R.; Dijkstra, M.; Manna, L. *Nat Mater* **2011**, *10*, 872.

(29) Rupich, S. M.; Talapin, D. V. *Nat Mater* **2011**, *10*, 815.

(30) Tessier, M. D.; Biadala, L.; Bouet, C.; Ithurria, S.; Abecassis, B.; Dubertret, B. *Acs Nano* **2013**, *7*, 3332.

(31) Baranov, D.; Fiore, A.; van Huis, M.; Giannini, C.; Falqui, A.; Lafont, U.; Zandbergen, H.; Zanella, M.; Cingolani, R.; Manna, L. *Nano Lett* **2010**, *10*, 743.

(32) Zanella, M.; Bertoni, G.; Franchini, I. R.; Brescia, R.; Baranov, D.; Manna, L. *Chem Commun* **2011**, *47*, 203.

(33) Talapin, D. V.; Nelson, J. H.; Shevchenko, E. V.; Aloni, S.; Sadtler, B.; Alivisatos, A. P. *Nano Lett* **2007**, *7*, 2951.

(34) Talapin, D. V.; Shevchenko, E. V.; Murray, C. B.; Kornowski, A.; Forster, S.; Weller, H. *J Am Chem Soc* **2004**, *126*, 12984.

(35) Carbone, L.; Nobile, C.; De Giorgi, M.; Sala, F. D.; Morello, G.; Pompa, P.; Hytch, M.; Snoeck, E.; Fiore, A.; Franchini, I. R.; Nadasan, M.; Silvestre, A. F.; Chiodo, L.; Kudera, S.; Cingolani, R.; Krahne, R.; Manna, L. *Nano Lett* **2007**, *7*, 2942.

(36) Smith, B. D.; Kirby, D. J.; Keating, C. D. *Small* **2011**, *7*, 781.

(37) Choi, J. J.; Bian, K. F.; Baumgardner, W. J.; Smilgies, D. M.; Hanrath, T. *Nano Lett* **2012**, *12*, 4791.

(38) Zhang, H.; Edwards, E. W.; Wang, D. Y.; Mohwald, H. *Phys Chem Chem Phys* **2006**, *8*, 3288.

(39) Talapin, D. V.; Shevchenko, E. V.; Kornowski, A.; Gaponik, N.; Haase, M.; Rogach, A. L.; Weller, H. *Adv Mater* **2001**, *13*, 1868.

(40) Zaitseva, N.; Dai, Z. R.; Leon, F. R.; Krol, D. *J Am Chem Soc* **2005**, *127*, 10221.

(41) Talapin, D. V.; Koeppe, R.; Gotzinger, S.; Kornowski, A.; Lupton, J. M.; Rogach, A. L.; Benson, O.; Feldmann, J.; Weller, H. *Nano Lett* **2003**, *3*, 1677.

(42) Menagen, G.; Mocatta, D.; Salant, A.; Popov, I.; Dorfs, D.; Banin, U. *Chem Mater* **2008**, *20*, 6900.

(43) Amirav, L.; Alivisatos, A. P. *J Phys Chem Lett* **2010**, *1*, 1051.

(44) Deka, S.; Falqui, A.; Bertoni, G.; Sangregorio, C.; Poneti, G.; Morello, G.; De Giorgi, M.; Giannini, C.; Cingolani, R.; Manna, L.; Cozzoli, P. D. *J Am Chem Soc* **2009**, *131*, 12817.

(45) Maynadie, J.; Salant, A.; Falqui, A.; Respaud, M.; Shaviv, E.; Banin, U.; Soulantica, K.; Chaudret, B. *Angew Chem Int Edit* **2009**, *48*, 1814.

(46) Luther, J. M.; Zheng, H. M.; Sadtler, B.; Alivisatos, A. P. *J Am Chem Soc* **2009**, *131*, 16851.

(47) Sadtler, B.; Demchenko, D. O.; Zheng, H.; Hughes, S. M.; Merkle, M. G.; Dahmen, U.; Wang, L. W.; Alivisatos, A. P. *J Am Chem Soc* **2009**, *131*, 5285.

(48) Jain, P. K.; Amirav, L.; Aloni, S.; Alivisatos, A. P. *J Am Chem Soc* **2010**, *132*, 9997.

(49) Demchenko, D. O.; Robinson, R. D.; Sadtler, B.; Erdonmez, C. K.; Alivisatos, A. P.; Wang, L. W. *Acs Nano* **2008**, *2*, 627.

(50) Robinson, R. D.; Sadtler, B.; Demchenko, D. O.; Erdonmez, C. K.; Wang, L. W.; Alivisatos, A. P. *Science* **2007**, *317*, 355.

(51) Peng, P.; Sadtler, B.; Alivisatos, A. P.; Saykally, R. J. *J Phys Chem C* **2010**, *114*, 5879.

(52) Carbone, L.; Kudera, S.; Giannini, C.; Ciccarella, G.; Cingolani, R.; Cozzoli, P. D.; Manna, L. *J Mater Chem* **2006**, *16*, 3952.

(53) Rippa, M.; Capasso, R.; Mormile, P.; De Nicola, S.; Zanella, M.; Manna, L.; Nenna, G.; Petti, L. *Nanoscale* **2013**, *5*, 331.

(54) Thorkelsson, K.; Nelson, J. H.; Alivisatos, A. P.; Xu, T. *Nano Lett* **2013**.

(55) Persano, A.; De Giorgi, M.; Fiore, A.; Cingolani, R.; Manna, L.; Cola, A.; Krahne, R. *Acs Nano* **2010**, *4*, 1646.

(56) Ryan, K. M.; Mastroianni, A.; Stancil, K. A.; Liu, H. T.; Alivisatos, A. P. *Nano Lett* **2006**, *6*, 1479.

(57) Singh, A.; English, N. J.; Ryan, K. M. *J Phys Chem B* **2013**, *117*, 1608.

(58) Li, L. S.; Alivisatos, A. P. *Adv Mater* **2003**, *15*, 408.

(59) Li, L. S.; Walda, J.; Manna, L.; Alivisatos, A. P. *Nano Lett* **2002**, *2*, 557.

(60) Lee, B.; Podsiadlo, P.; Rupich, S.; Talapin, D. V.; Rajh, T.; Shevchenko, E. V. *J Am Chem Soc* **2009**, *131*, 16386.

(61) Urban, J. J.; Talapin, D. V.; Shevchenko, E. V.; Murray, C. B. *J Am Chem Soc* **2006**, *128*, 3248.

(62) Bian, K. F.; Choi, J. J.; Kaushik, A.; Clancy, P.; Smilgies, D. M.; Hanrath, T. *Acs Nano* **2011**, *5*, 2815.

(63) Choi, J. J.; Bealing, C. R.; Bian, K. F.; Hughes, K. J.; Zhang, W. Y.; Smilgies, D. M.; Hennig, R. G.; Engstrom, J. R.; Hanrath, T. *J Am Chem Soc* **2011**, *133*, 3131.

(64) Hanrath, T.; Choi, J. J.; Smilgies, D. M. *Acs Nano* **2009**, *3*, 2975.

(65) Baker, J. L.; Widmer-Cooper, A.; Toney, M. F.; Geissler, P. L.; Alivisatos, A. P. *Nano Lett* **2010**, *10*, 195.

(66) Pietra, F.; Rabouw, F. T.; Evers, W. H.; Byelov, D. V.; Petukhov, A. V.; Donega, C. D.; Vanmaekelbergh, D. *Nano Lett* **2012**, *12*, 5515.

APPENDIX A

INSTRUMENTAL AND ANALYTICAL METHODS FOR CHAPTER 2

Device Fabrication. Field-effect transistors were lithographically patterned according to reported protocols.[47] The gate electrode was deposited by thermally evaporating 10 nm of Al and 70 nm of Au onto the etched backside of a p-doped silicon wafer (0.02 (ohm-cm)). Source and drain electrodes were deposited by thermally evaporating Cr/Au (2.5 nm/32.5 nm) onto a 300 nm thermally grown oxide on the wafer front followed by lift-off of the photoresist mask. The channel length was varied from 100 to 150 μm and the channel width from 3 to 4 mm. Prior to substrate priming and NC deposition, the wafers were cleaned by sonication for 10 minutes each in acetone and 2-propanol before drying and cleaning by UV-ozone treatment (30 minutes).

Electron Microscopy. Transmission electron microsocopy (TEM) characterization was performed on an FEI Tecnai T12 operating at 120 kV. Due to the caustic nature of the ligand chemistry, all samples for electron microscopy were deposited on silicon nitride windows instead of carbon coated metal grids. A dilute (1 mg/mL) NC dispersion in TCE was drop cast onto a silicon nitride window. The silicon nitride window was submerged briefly (30 minutes) in a dilute solution of hydrazine in acetonitrile before being treated in the ChaMs for 20 minutes. The windows were carefully handled and rinsed before positioning on top of a clean silicon wafer and annealed on a hot plate using the same protocol for ligand exchange. A minimum of 200 particles were analyzed for statistical analysis. Scanning electron microscopy

(SEM) characterization of PbSe-ChaM composites deposited on MPTMS coated Si substrates was performed on a LEO-1550-FESEM.

Optical Absorption Spectroscopy. Optical absorption spectra of NC dispersions were recorded with a Cary 5000 UV-Vis NIR spectrophotometer at 2 nm spectral bandwidth. Absorption spectra of PbSe NC dispersions were taken in a quartz liquid cell. Solid state samples were drop cast from diluted (5 mg/mL) NC solutions in 4:1 octane-hexane onto MPTMS-functionalized glass or quartz slides and dried slowly in a controlled solvent-vapor environment before subjecting to ligand exchange and treatment.

Infrared Absorption Spectroscopy. All spectra were gathered in transmission mode on a Bruker-Hyperion-FT-IR Microscope. Solid state samples were drop cast from diluted (5 mg/mL) NC solutions in 4:1 octane-hexane onto MPTMS-functionalized glass or quartz slides and dried in a controlled environment before subjecting to ligand exchange and treatment.

X-ray Diffraction. X-ray diffraction patterns were collected on a Scintag Theta-Theta X-ray diffractometer operating with Cu-Kα radiation. Sample preparation was analogous to that for UV-Vis absorption spectroscopy, with the exception that silicon substrates were used instead of glass slides. The average crystallite size was calculated from the width of the (200) reflection by using the Scherrer equation.

Grazing-incidence Scattering. Grazing incidence small angle X-ray scattering (GISAXS) measurements were performed on beam line D1 of the Cornell High Energy Synchrotron Source (CHESS) using monochromatic radiation of wavelength λ = 1.117 Å with a bandwidth Jλ/λ of 1.5%. The X-ray beam was produced by a

hardbent dipole magnet of the Cornell storage ring and monochromatized with Mo:B4C synthetic multilayers with a period of 30 Å. The D1 area detector (MedOptics) is a fiber-coupled CCD camera with a pixel size of 46.9 μm by 46.9 μm and a total of 1024 × 1024 pixels with a 14-bit dynamical range per pixel. Typical read-out time per image was below 5 s. The images were dark current corrected, distortion-corrected, and flat-field corrected by the acquisition software. The sample to detector distance was 946 mm, as determined using a silver behenate powder standard. The incident angle of the X-ray beam was

varied from 0.25 to 0.5° i.e., slightly above the silicon critical angle. Typical exposure times ranged from 0.1 to 1.0 s. Scattering images were calibrated and integrated using the Fit2D software. GISAXS diffraction peaks were indexed and fitted using in-house software.2

After well-ordered GISAXS images were obtained, GIWAXS patterns on the same sample spot were recorded on Fuji image plates, and scanned for digital processing with a GE Healthcare Typhoon FLA-7000 image plate reader. Image plates were letter sized with 2000 x 2500 pixels and a 100 μm pixel size. For typical exposures of 2s an image plate was placed in a holder at 180 mm from the sample; the holder could be quickly slided in and out of scattering position on a rail. The intense scattering close to the direct beam was blocked with lead tape. Digital images were also analyzed using Fit2D.

Electrical Measurements. All electrical measurements were performed using a homemade probe station in nitrogen glove box with Keithley 2400 and Keithley 6430 source meters.

APPENDIX B

INSTRUMENTAL AND ANALYTICAL METHODS FOR CHAPTER 3

Electron Microscopy. Transmission electron micrographs were collected on an FEI Tecnai T12 operating at 120 kV. Scanning electron micrographs were recorded on a LEO-1550-FESEM.

Photoluminescence Emission. A 420 nm tunable diode laser served as the light source for photoluminescence (PL) emission studies. A sample with standing rods were used for all experiments. The excitation beam was shone perpendicular to the sample substrate. A monochromator and detector was placed 90 degrees to the excitation beam. A linear polarizer was positioned between the sample and the detector to vary the polarization. A half wave-plate was placed between the polarizer and the detector. With every corresponding rotation of the polarizer, the half wave-plate was rotated accordingly such that the polarization of light entering the grating and the detector is kept constant.

Photoluminescence Excitation. A 420 nm tunable diode laser served as the light source for photoluminescence (PL) emission studies. A clean 1 cm x 1 cm glass substrate cast with standing rods were used for all experiments. The excitation beam was directed perpendicular to the sample substrate. A monochromator and detector was placed 90 degrees to the excitation beam. A linear polarizer was positioned between the sample and the detector to vary the polarization. A half wave-plate was

placed between the polarizer and the detector. With every corresponding rotation of the polarizer, the half wave-plate was rotated accordingly such that the polarization of light entering the grating and the detector is kept constant.